Title
Ab-initio simulation studies of chromium solvation in molten fluoride salts

Authors
Winner, Nicholas
Williams, Haley
Scarlat, Raluca O
et al.

Publication Date
2021-08-01

DOI
10.1016/j.molliq.2021.116351

Peer reviewed

Journal of Molecular Liquids 335 (2021) 116351

Contents lists available at ScienceDirect

Journal of Molecular Liquids

journal homepage: www.elsevier.com/locate/molliq

Ab-initio simulation studies of chromium solvation in molten fluoride salts

Nicholas Winner [a,b], Haley Williams [c], Raluca O. Scarlat [c], Mark Asta [a,b,*]

[a] Department of Materials Science and Engineering, University of California, Berkeley, CA 94720, USA
[b] Materials Sciences Division, Lawrence Berkeley National Laboratory, Berkeley, CA 94720, USA
[c] Department of Nuclear Engineering, University of California, Berkeley, CA 94720, USA

ARTICLE INFO

Article history:
Received 29 October 2020
Revised 22 April 2021
Accepted 27 April 2021
Available online 4 May 2021

Keywords:
Molten salts
Ab initio molecular dynamics
Solvation
Solutes
Fluoroacidity

ABSTRACT

Understanding molten salt chemistry is essential in ongoing research of the molten salt nuclear reactor (MSR). In this context, detailed understanding of the mechanisms underlying selective oxidation of metal species, such as Cr, is required to guide the design of effective corrosion mitigation strategies in molten salts. An important starting point for such mechanistic understanding is knowledge of the solvation structure and its role in controlling metal speciation. In this work, we use ab initio molecular dynamics simulations to study the short-range (on the scale of the nearest-neighbor bond lengths) and medium-range (over length scales of several neighbor spacings) structure in three different fluoride melts with and without Cr addition; namely, 2KF-NaF, 2LiF-BeF_2, and 3LiF-AlF_3. We find that Cr^0, Cr^{2+}, Cr^{3+} can each be coordinated by different numbers of F^-, with the variance in coordination number decreasing as oxidation state increases, and that these coordination geometries are largely independent of solvent. The manner by which Cr changes the medium-range structure, however, is found to be solvent-dependent. While 2KF-NaF melts show short and medium range order that is highly dynamic, 2LiF-BeF_2 and 3LiF – AlF_3 are characterized by molecular associates that are relatively long-lived that organize into oligomer structures on larger length scales. Rather than being solvated by F^- ions alone, we find that Cr can incorporate into and be solvated within this oligomer structure. Fluoroacidity, alone, may therefore prove too simple a metric for assessing the corrosivity of molten fluorides. As our work suggests, the ability of Cr to solvate must be understood in the context of the short- and medium-range structure of the solvent.

1. Introduction

Molten halide salt mixtures have been studied extensively for a variety of nuclear engineering applications including use in the pyroprocessing of nuclear waste [1] and as a potential coolant and/or fuel carrier in nuclear reactors [2–4]. Investigation of molten fluorides for nuclear reactor technology began in the 1950s and 1960s with the Aircraft Reactor Experiment (ARE) [5] and the subsequent Molten Salt Reactor Experiment (MSRE) [6]. With renewed interest in molten salt nuclear reactor design from expert communities such as the Generation IV Forum [7], expanded attention has been devoted to the pursuit of a fundamental understanding of molten salt chemistry. Understanding the molecular structures that form in the high temperature ionic molten fluorides is instrumental in developing a mechanistic understanding of the thermo-physical and thermo-chemical properties of these fluids as coolants and as solvents.

Of particular interest is the solvation of chromium in molten fluorides, which is present as an alloying element in structural materials used in MSRs and fluoride salt-cooled high-temperature reactors (FHRs). Compared to other common elements in these materials (such as Fe, Ni, or Mo), Cr more readily oxidizes to a fluoride and dissolves in the salt melt [8]. The MSRE identified dissolved Cr in fuel salt as the best indicator of corrosion progress [6]. Research on the corrosion of Ni-Cr alloys in LiF-NaF-KF has demonstrated the selective dealloying and dissolution of Cr as the predominant corrosion mechanism [9–12]. Furthermore, dissolved Cr is postulated to increase the near-infrared absorption coefficient of the salt, affecting radiative heat transfer in some otherwise-transparent melts, as demonstrated in measurements of heat transfer [13] and in the modeling of LiF and LiF-NaF-KF melts [14]. Despite the practical relevance of Cr solvation in molten salts, fundamental understanding of its speciation in these solvents remains incomplete.

* Corresponding author at: Department of Materials Science and Engineering, University of California, Berkeley, CA 94720, USA.
E-mail address: mdasta@berkeley.edu (M. Asta).

https://doi.org/10.1016/j.molliq.2021.116351
0167-7322/

There has been much work to date on understanding the thermodynamics of Cr dissolution in molten fluorides. Several reports from the Aircraft Nuclear Propulsion Project documented the solubility and equilibrium concentration of CrF_2 in various molten fluoride mixtures [15–19]. Notably, these reports show that Cr^{2+} is the seemingly stable valence state in LiF-ZrF_4, NaF-ZrF_4, KF-ZrF_4, and RbF-ZrF_4, and that the equilibrium concentration of CrF_2 at 600 °C varies distinctly with the solvent chemistry [18,17,20]. The speciation of Cr corrosion products in molten LiF-NaF-KF salt was further studied by Qiu et al., who found the predominant oxidation state to be Cr^{3+} [21]. This difference in the predominant oxidation state was attributed to the molten salt's *fluoroacidity*. Briefly, the metric of fluoroacidity (pF) is defined by the activity of F^- in the melt (a_{F^-}):

$$pF = -log(a_{F^-}) \quad (1)$$

where a_{F^-} is measured relative to an appropriate reference state, such as F_2 gas at 1 atm partial pressure. A salt which is a weak fluoroacid/strong fluorobase will have a high activity of F^-. The authors of Ref. [21] contend that, because of the fluorobasicity of LiF-NaF-KF, the higher valence Cr^{3+} can be stabilized by complexation with the available F^-, decreasing its chemical activity and consequently increasing the observed concentration of Cr^{3+} in the melt. For further explanation of this Lewis acid/base behavior, the reader is referred to [22].

In the ARE, the disproportionation of Cr^{2+} to Cr^{3+} and Cr^0 was found to depend on the concentration of ZrF_4 in a $LiF - NaF - ZrF_4$ melt (NaF:LiF held at 40:60, 800°C) [23]. In melts with more of the fluoroacidic ZrF_4, less dissolved chromium was present as Cr^{3+}, indicative of the competition between Zr^{4+} and Cr^{3+} for fluoride ions. Similar tests were performed with ZrF_4 additions to LiF-BeF_2 (48–52 mol%) and LiF-BeF_2-ThF_4 (67–23-10 mol%) to investigate the differences of a salt presumably less fluoroacidic (BeF_2) than ZrF_4. It was shown that BeF_2-containing melts are more fluorobasic than the corresponding ZrF_4 mixtures and that a higher ratio of Cr^{3+}/Cr^{2+} is found in the more fluorobasic mixtures. Similar results are shown in [24], where authors demonstrate, by Raman studies, that addition of fluorobasic LiF to 2LiF–BeF_2 leads to Cr^{2+} disproportionation to Cr^{3+} (solvated as CrF_6^{3-}).

The solvation structure in molten salts is directly related to the thermodynamics of dissolution: in order for corrosion products (e.g. Cr^{2+}) to dissolve into the melt, they must become solvated by F^- ions in their first coordination shell. The connection between structure and thermodynamics is highlighted in the quasi-chemical model [25–28], which formulates free energies using coordination complexes and the resultant first- and second-nearest neighbor environments as the system components, and has been applied to describe the thermodynamics of molten fluorides [29]. Beyond the first coordination shell, which we refer to as the local or short-range structure, is the medium-range structure of molten salts. The canonical example of medium-range order in molten salts is their "network formation." For example, in $LiF - BeF_2$, it was observed that tetrahedrally coordinated BeF_4^{2-} complexes are linked by bi-coordinated F^- anions [30,31], into structures that we will refer to as oligomers in what follows. This medium-range structure is not exclusive to $LiF - BeF_2$, and many salts exhibit this behavior if they contain a cation which forms strong coordination complexes with F^-, for example $LiF - ZrF_4$ [32].

The structure of molten salts has been well documented in previous studies, with a research history that extends many decades [33–35,31]. However, the mechanism by which Cr incorporates into the existing structure of a molten salt is still incompletely understood. Arguments based on fluoroacidity, which would describe the ability of Cr to solvate in terms of the availability of free fluoride ions, are attractive, as they are agnostic to the details of the salt chemistry, but remain unproven. If Cr can, for example, share fluoride ions with the solvent by integrating into the existing oligomer structure, then the need for a fluorobasic salt to stabilize higher oxidation states is not obvious. Understanding the structure of Cr in molten fluorides is the first step toward developing a mechanistic understanding of how Cr dissolves into the salt and becomes solvated within them.

Current understanding of molten salt structure, at both short- and medium-range scales, has been invaluably aided by the use of molecular dynamics (MD) simulations. Such molecular-scale simulations have been widely employed to probe structural, dynamic, spectroscopic, and thermodynamic properties [43,44,39,38,41,30,36,45,42,40,37,46–49]. For a thorough survey of such studies, the reader is referred to [50]. With the increasing availability of high performance computing resources, ab initio molecular dynamics (AIMD) has been applied more recently to a variety of molten salt research problems. While requiring significantly more computational resources than simulations based on classical force fields, AIMD is applicable to different salt mixtures without the need to develop new interatomic potentials. It has been successfully used to study the behavior of molten salt structure [52,51] as well as the structural, thermodynamic, and transport properties of common corrosion products [53,54]. Nam et al. specifically investigated some features of the local structure and the transport of Cr in molten $2LiF - BeF_2$ and $LiF - NaF - KF$ with AIMD [55]. The present work builds on this previous study by expanding the analysis to more salt solvents and medium-range structure, to further advance the understanding of solvation and speciation of Cr solute in molten fluoride mixtures.

Specifically, we employ AIMD in the present work to study the short- and medium-range structure in three binary fluoride melts with and without added Cr solutes. Namely, we study 2KF-NaF, $2LiF - BeF_2$, and $3LiF - AlF_3$ with and without the addition of Cr^0, Cr^{2+}, and Cr^{3+}. $2LiF - BeF_2$ was selected for its technological relevance to interpretation of MSRE data and to design of contemporary MSRs and FHRs, while 2KF-NaF and $3LiF - AlF_3$ were selected to compare among Cr solvation in salts with monovalent, divalent, and trivalent cations. These mixtures were also selected to compare across solvents expected to cover a range of fluoroacidities [98–100].

2. Methods

2.1. Compositions of Molten-Salt Mixtures Investigated

The composition of each salt mixture is selected such that the strongly complexing cation would be nominally fully coordinated. Be^{2+} is nominally 4-fold coordinated, and so the ratio of LiF to BeF_2 was chosen as 2:1. Similarly, Al^{3+} is nominally 6-fold coordinated, and so the ratio of LiF to AlF_3 was chosen as 3:1. In the case of 2KF-NaF, whether complexes would form was not clear. Initial simulations suggested that the coordination number of both Na and K is 4-fold, but with K having a much higher variance (see Section 3.1.2). The K:Na was chosen as 2:1. Given these mixing ratios, we constructed simulation cells with 96 atoms for 2KF-NaF, 98 for 2LiF-BeF_2, and 100 for 3LiF-AlF_3. The system size for each simulation cell was chosen such that the radial distribution function (RDF) reached a value close to unity (i.e., indicating lack of significant correlation) within half the largest periodic length, to avoid significant artifacts from the periodic boundary conditions. Representative snapshots for equilibrated samples of 2LiF-BeF_2 and 2KF-NaF are shown in Fig. S1.

For systems containing Cr, charge neutrality was maintained by removing cations rather than adding F^- anions to compensate the Cr charge. This choice was made to facilitate the study of the intrinsic competition for F^- between different cations in the salt, and for this purpose the ratio of F^- to the cations that form the dominant complexes (Na, Be, Al) should not be changed. In each solvent, we determined which cation complexed more weakly with F^- and removed that species in the amount necessary to balance the charge of the desired Cr oxidation state. Specifically, Li was removed in $2LiF-BeF_2$ and $3LiF-AlF_3$ mixtures, while K was removed in 2KF-NaF.

2.2. Simulation details

Prior to the AIMD simulations, initial equilibration runs were performed using Born–Meyer-Huggins classical force fields, with parameters taken from Refs. [30,36]. We note that in the case of Cr, no appropriate parameters were found in the literature, and for this species we chose to use the short-range term for Zr, while changing the atomic charge as needed, and neglecting polarization, as was done for transition metals in the aforementioned references. We stress here, that these force fields were only used to obtain an initial structure for the AIMD simulations, in order to reduce the time needed for them to equilibrate; all of the results presented below were derived from the subsequent AIMD simulations. In the classical simulations we began by generating random structures using Packmol [56] and then equilibrated the systems using LAMMPS [57]. An initial 5 ps NVT simulation at the experimental density was performed using a Langevin thermostat to raise the temperature to 700 °C. After this initial equilibration we conducted an additional 50 ps NPT simulation using a Nose–Hoover [58,59] thermostat (at 700°C) and barostat (with zero external pressure), allowing the dimensions of the simulation cell to expand/contract, while retaining the cubic shape. We determined the equilibrium density from the average of the last 25 ps. Finally, we ran an additional 50 ps NVT simulation with a Nose–Hoover thermostat at this density.

Following the steps described above, AIMD simulations were performed using the final structures from the classical simulations as input. First, the equilibrium volume was determined via a direct descent approach. Short 1 ps simulations were run to determine the cell pressure, the dimensions of the cell were then automatically adjusted toward zero pressure and rerun. This procedure was repeated until the final pressure on the cell ranged between −5 and 5 kbar. These newly equilibrated structures were then used for production AIMD simulations, employing Nose–Hoover NVT dynamics with an unchained thermostat temperature of 700°C.[1] A Nosé-mass corresponding to period of 40 time steps was chosen. The performance of the thermostat is shown in Fig. S2, which demonstrates excellent agreement between the velocity (speed) distributions in the simulations and the analytical results from Maxwell–Boltzmann statistics. We note that at this temperature, which was selected to reproduce the operating conditions of the MSRE, the molten phases for 2KF-NaF and $3LiF-AlF_3$ mixtures are metastable. This is not a concern for the present studies since the timescale for nucleation of solids is expected to be much greater than that of the AIMD simulations, such that the intrinsic properties of the molten states for these mixtures can be probed straightforwardly.

The AIMD simulations were performed within the framework of electronic density-functional theory (DFT) using the Vienna Ab-Initio Simulation Package (VASP) with the projector augmented wave (PAW) method [61,60], a plane wave basis set, and the Perdew-Burke-Ernzerhof (PBE) generalized-gradient-approximation (GGA) exchange correlation functional [62]. The PAW potentials employed were Li ($2s^1$), Be ($2s^2$), F($2s^22p^5$), Na ($3s^1$), K_sv ($3s^23p^64s^1$), Al ($3s^23p^1$), and Cr($3d^54s^1$). Calculations were performed using a single (gamma) k-point, 600 eV plane wave cutoff, and a 1e-7 eV convergence criteria for electronic self-consistency. We additionally accounted for the effect of dispersion interactions, which was shown in previous studies to be necessary to accurately reproduce the salt density [55], using the D3 formulation by Grimmes [63]. NVT simulations were performed for 38–51 ps, with 5 ps of equilibration, for each salt mixture using a timestep of 2 fs. All calculations were performed allowing for spin polarization; while this was necessary for the systems containing Cr solutes, due to the finite local moments of this species, we expect that the results for the pure solvent mixtures (without Cr) would have been identical if computed spin-averaged. For the simulations with Cr included, we verified that this solute species did not change its oxidation state by tracking the magnetic moment of the system; we observed only a few instances in the thousands of simulation steps where the magnetic moment changed, but this was always followed by immediately returning to the initial value in the next step.

From the AIMD simulations for each of the salt mixtures considered, both with and without Cr solute included, detailed structural analyses were performed. The methods used to probe the structure on short and medium length scales are described in the next three sub-sections.

2.3. Radial Distribution Functions

RDFs ($g_{\alpha\beta}$) between species α and β were calculated as:

$$g_{\alpha\beta}(r) = \frac{1}{\frac{4}{3}\pi((r+\Delta r)^3 - r^3)} \frac{1}{N_\alpha \rho_\beta} \langle \sum_{i=1}^{N_\alpha} N_{i\beta}(r) \rangle \quad (2)$$

where r is the inter-particle distance, N_α and N_β are the number of α and β atoms in the simulation cell, respectively, ρ_α and ρ_β are the corresponding number densities, Δr is the histogram bin width, $N_{i\beta}(r)$ denotes the number of β neighbors of atom i in a bin centered at r, and $\langle . \rangle$ denotes time averaging. Using these RDFs, the nearest-neighbor (NN) coordination numbers ($N_{\alpha\beta}$) were computed as:

$$N_{\alpha\beta} = 4\pi\rho_\beta \int_0^R r^2 g_{\alpha\beta}(r) dr \quad (3)$$

where R is the first-coordination shell radius (FCSR), defined as the position of the minimum in the partial RDF beyond the first peak for the specific type of pair considered. The NN coordination number (CN), $N_{\alpha\beta}$, is the time-averaged number of β neighbors of α within this FCSR.

For the analysis of cation-cation order for Cr-containing salt in Section 3.2, we will make use of a decomposition of the RDFs in terms of shared neighbors by following the approach described in Ref. [64]. Specifically, we decompose the RDFs according to whether or not two cations share a common neighbor, which we call intra-oligomer, if they do not share a common neighbor, which we call inter-oligomer, or if the two cations participate in direct bonding. We refer to this decomposed RDF as $g^{\gamma}_{\alpha\beta}(r)$, where γ refers to one of three aforementioned conditions. The criteria for determining common-neighbors is described below.

2.4. Solvation Structure Correlation Times

Cage correlation functions (CCFs) were calculated in order to quantify the dynamics of coordination complexes within the salts.

[1] For the AIMD simulations the velocities of the atoms were re-initialized using a Boltzmann distribution and ensuring zero center of mass velocity.

In this work the CCFs define the probability that a given NN coordination complex remains unchanged after a given period of time [65,95]. For the systems considered here, coordination complexes form between cation and anion species, and may change by gaining, losing, or exchanging a coordinating F^- anion. The CCF is calculated as:

$$C_{M^{x+}}(t) = \frac{1}{N_{M^{x+}}} \langle \sum_{i=1}^{N_{M^{x+}}} \sum_{j=1}^{N_{F^-}} 1 - n_{ij}^{in/out}(t_0, t_0+t) \rangle_{t_0} \quad (4)$$

where M^{x+} is the cation being coordinated by F^- anions, $\langle \cdot \rangle_{t_0}$ indicates averaging over time origins, t_0, and $n_{ij}^{in/out}(t_0, t_0+t)$ indicates whether a neighbor j for atom i has changed between t_0 and $t+t_0$. Using the notation $l_i(t)$ as the neighbor list for cation i at time t, and letting $l_i(t)$ only consist of neighbors within the first coordination shell:

$$n_{ij}^{in/out}(t_0, t_0+t) = \begin{cases} 1 & j \in l_i(t_0),\ \notin\ l_i(t_0+t) \\ 1 & j\ \notin\ l_i(t_0), \in l_i(t_0+t) \\ 0 & else \end{cases} \quad (5)$$

Using the two "if" conditions in Eq. 5, one can also construct CCFs that look exclusively at coordination numbers changing by dissociation or by capture of F^- ions. We have neglected this distinction here, as longer MD simulations would be required to ensure proper statistical sampling.

The calculated CCFs are normalized so that $C_{M^{x+}}(t=0) = 1$, and fit assuming an exponential decay:

$$C_{M^{x+}}(t) = e^{\frac{-t}{\tau}} \quad (6)$$

where τ is the exponential decay constant referred to in what follows as the correlation time. In order to improve our fit, we used weighted regression with $\frac{1}{\sigma}$ as the weights, where σ is the standard deviation of the CCF for a given time interval. The value of τ represents the time for approximately 63 % $(1 - \frac{1}{e})$ of the $\alpha\beta$ coordination complexes to change their state. A high value of τ indicates a stable, long-lived associate.

2.5. Coordination and Molecular Distributions

We examined the short and medium range structures of the simulated salt mixtures by investigating a series of distributions. Here, when referring to short-range (or local) structure, we mean the first nearest-neighbor (FNN) environment characterizing the coordination of cation species by F^- anions. By medium-range order we refer to ordering beyond FNN distances. This includes the second-nearest-neighbor (SNN) arrangement of cations and the shared connections between their coordination shells, as well as the organization of molecular associates into oligomers over SNN and larger length scales.

To characterize FNN coordination environments we make use of two approaches. The first is to use Eq. 3 to compute the NN CNs, as described in subSection 2.3. In the second approach (see Section 3.2.1), we use the methodology in [66] in which the coordination number of a particular cation is defined as the weighted average of the solid angles swept out by the Voronoi facets surrounding it (for more details, see [66]). We employ this approach to analyze the statistics of the CNs, and in so doing we make use of bi-variate scatter plots and corresponding marginal distributions showing the frequency of a particular cation having a given NN coordination and a mean separation from its nearest neighbors. Hereafter we refer to these bi-variate scatter plots simply as joint distributions.

We investigate medium-range order by constructing molecular graphs based on the FCSR corresponding to a given cation-F^- pair. Then we construct a graph of each snapshot by allowing each cation species to be a node (vertex), and constructing edges (links) between metal coordination centers based on whether or not the F^- lie in the FCSRs of the vertices. Each connected sub-graph in the overall graph of the snapshot define an oligomer. When constructing the graph for each snapshot, we assume that oligomers must be formed by strongly associating cations, e.g. Be^{2+} in 2LiF-BeF_2, as discussed in Section 3.1.2.

The isolated oligomers are analyzed for their size by counting the number of cation centers and coordinating F^-. We also count the frequency of n-atom common neighbor connections (CNCs). By this, we mean that for each pair of cations in an oligomer, we consider the FNNs of each cation, and calculate their intersection. If the intersection is non-empty, the two cations are second-nearest neighbors (SNNs), and the length of this intersection is the number of CNCs, which we refer to as 1-atom (vertex sharing), 2-atom (edge sharing), or 3,4-atom (face sharing).

3. Results

3.1. Solvent structure

In this section we characterize the structure of the pure (i.e., without addition of Cr solutes) solvent salt mixtures on short and medium-range scales. We begin with a comparison to previously published experimental and simulation results for 2LiF–BeF_2 to establish the accuracy of the methods described above. We then move on to a comparison of the FNN coordination structure across salt solvents, and then focus on the CNCs and oligomer distributions that characterize medium-range order. The results introduce the key features of the solvent structures in the salt mixtures, and provide base-line structural characteristics that are used in the following section to analyze Cr solvation, as well as the changes that this solute induce in the solvent structure.

3.1.1. Benchmarking comparisons for $2LiF - BeF_2$

Several prior studies of $2LiF - BeF_2$ structure have been performed experimentally [67–69] and computationally [30,70,55,53]; they are compared to the present results in Table 1. The data from the present work in this Table are obtained from the RDFs shown in Fig. 1, which also presents data for the other salt solvents discussed in the next subsection. In Fig. 1 the first-peak locations are determined to be 1.55Å for Be-F, 1.85Å for Li-F and 2.58Å for F-F. We identify a small shoulder in the F-F correlation at 3.10Å, which was also observed in an X-ray diffraction study performed at 750^0C, at a radial distance of 3.02Å [71]. Previous simulation results for RDFs at 700 °C were generated using classical force fields [70] and AIMD simulations [55]. Other studies that include LiF and BeF_2 and use classical simulations show qualitatively similar results, but are excluded from the comparison in Table 1 because they either contain other salt constituents (e.g. $2LiF - BeF_2 - ThF_4$) [46,72] or study a different composition than the 2:1 LiF:BeF_2 ratio considered here [73]. The equilibrium density of $2LiF - BeF_2$ derived from the current simulations is 2.1(3) g/cm^3 at 700 °C [2]. Previous computational studies have reported a range of 1.92–1.986 g/cm^3 (see, e.g., Table 1). The 1988 NIST database value for $2LiF - BeF_2$ is 1.937(6) g/cm^3 [74], and the experimental value of 1.89 g/cm^3 listed in Table 1 is taken from the diffraction study in [71]. Similarly, for $3LiF - AlF_3$, we compute a density of 2.08(30) g/cm^3 and experimental estimates based on molar additivity report 2.3(2) g/cm^3 [75].

[2] The error bar reported here follows from [53] as the propagation of uncertainty resulting from having a pressure-convergence criteria of ± 5 kbar in determining the equilibrium volume

Table 1
Comparison of structural parameters and density obtained in this work for 2LiF – BeF_2 at 700 °C with results reported in previous studies.

Ion Pair	First Peak Radius (Å)				Coordination Number			
	Exp.[1]	PIM	AIMD	This Work	Exp.[1]	PIM	AIMD	This Work
Be-F	1.58(1)	1.58	1.55	1.55	4.0(5)	4.0	4	3.9
F-F	2.56(6)[2]	2.61	2.58	2.58[2]	3(1)[2 3]	11.3	12	12
	3.02(2)[2]			3.10[2]	5(1)[2 3]			
Li-F	1.85(2)	1.81	1.88	1.85	4.0(1)	4.0	4.7	4.4
Density (g/cm^3)	1.89	1.96[4]	1.97	2.1(3)				

[1] The label "Exp." corresponds to X-ray diffraction results at 750 °C [71], "PIM" corresponds to calculations using the polarizable ion model at 700 °C [30], and previous AIMD results at 700 °C come from [55].
[2] Where two values are reported, one below the other, in the case of the F-F pair, the second number corresponds to the shoulder of the first peak.
[3] The discrepancy in the F-F CN versus that reported in [71] is most likely caused by the different methodologies used in their calculations. In this work CN values were obtained by integrating the RDF to the FCSR. By contrast, in the analysis of the experimental data in [71] use was made of a deconvolution of the diffraction data employing sums of Gaussians; the two experimental CN values obtained from this analysis correspond to the contributions including the first peak and the first peak and shoulder, respectively.
[4] This density was used as input to PIM study, not derived from the PIM simulations directly.

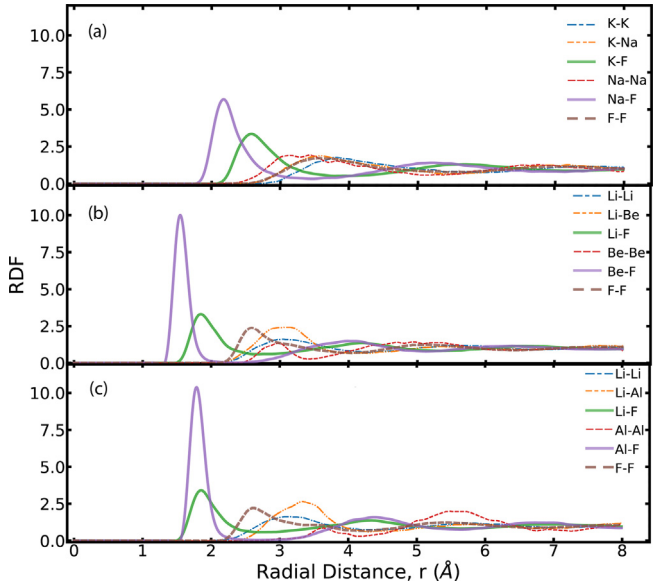

Fig. 1. Radial distribution functions. (a) 2KF-NaF (b) 2LiF – BeF_2, (c) 3LiF – AlF_3.

We determine the Be-F FCSR to be 1.92Å, leading to a CN of 3.9. This is smaller than the nominal CN value of 4 that is commonly assumed, and is reported in previous experimental and simulation investigations, as summarized in Table 1. We acknowledge that there is some uncertainty in the exact value of the FCSR in our simulations, and if we extend the FCSR to 2.14Å the CN increases to a value of 4.0. We thus acknowledge that the CN from the current simulations could be slightly higher than 3.9, due to the uncertainty in the precise value of the FCSR, although a value for the FSCR of 2.14Å seems too large to be associated with Be-F bonding. Thus the present simulations do suggest a CN smaller than the nominal value of 4, implying that a fraction of the Be atoms are under-coordinated in the simulations, as we discuss further below. In the case of Li-F we find a CN of 4.4, which is intermediate between the value of 4.7 obtained in previous AIMD work [55], and 4 reported based on classical simulations [70] and experimental measurements [71]. For F-F the CN value of 12 obtained here at the FCSR for g_{FF} (located beyond the shoulder of after the first peak) agrees with previous AIMD simulation results and is close to the previous classical simulations. However, all of the simulation results for F-F coordination number are significantly larger than the experimental value of 5 obtained including the peak and shoulder contributions, from the method used to deconvolve the measured diffraction data into the F-F partial RDFs. Further analysis is required to understand the orgin of this discrepancy between the analysis of the experimental data and simulation results for the case of the F-F CN.

The cage correlation time, τ, for BeF_4^{2-} complexes is computed here to be $\sim$ 25 ps (see Table 2 for comparison with other ion pairs). Salanne et al. calculated a comparable but slightly smaller value of τ=18 ps using longer classical molecular dynamics simulations [70]. The difference between the two values likely originates from a combination of the comparatively smaller sampling statistics in our study (and hence larger statistical uncertainties) and the sensitivity of τ to the exact value of the FCSR. We tested the sensitivity of τ to the choice of the Be-F FCSR by varying it from 1.7 to 2Å, and found that this choice can change τ from 16 ps to 27 ps. Thus, the ambiguity in the first-coordination shell cut-off used to calculate the CCFs introduces an uncertainty that is on the order of 11 ps. While we are not aware of previous studies of the cage correlation times for 3LiF-AlF_3 and 2KF-NaF, we note some qualitative agreements. Similarly to the observations made here for 2KF-NaF, Raman studies of LiF-KF indicate sub-picosecond lifetimes (0.3 ps) for anion-cation associates [76], while high temperature liquid NMR data for NaF-AlF_3 indicates the presence of a combination of dissociated, bridging, and strongly-associated non-bridging F [77].

From these bench-marking comparisons, we conclude that the static and dynamic structures, as characterized by the RDFs and cage-correlation times, for 2LiF-BeF_2 are consistent between the current and previous simulation results, within the uncertainties reported here. A notable exception is the CN value for Be-F that is slightly lower than 4 in the current simulations. In comparison to data reported from experimental measurements, a comparable level of agreement is obtained, with the exception of the F-F coordination number that shows significantly larger values in both the present and previous simulation results. Further detailed comparisons between the current and previous theoretical and simulation results for 2LiF-BeF_2 will be considered below in the context of medium-range structure, as characterized by oligomer size distributions.

3.1.2. FNN cation–anion coordination: strong and weak associates

We consider next a comparison of the cation–anion fist-nearest neighbor (FNN) coordination structures across the different salt mixtures. We begin by comparing the FNN peaks in the RDFs in Fig. 1, and note that the strongest peaks correspond to Be-F and Al-F in 2LiF-BeF_2 and 3LiF-AlF_3, respectively. Each of these peaks are separated from the rest of the RDF by a region of vanishing probability, indicating well-defined FNN coordination complexes. By contrast, the FNN peaks in the Li-F RDFs for both 2LiF-BeF_2 and 3LiF-AlF_3 are much more diffuse (i.e., much broader and less

Table 2
Characteristic cation–anion cage-correlation times (in ps) obtained from fitting τ in Eq. 6. Error bars are one standard deviation; uncertainty with respect to cutoff radius (see text for details) are not included in this. Be-F and Al-F are categorized as strong associates. The alkaline fluorides form weak associates with $\tau < 1ps$.

2KF – NaF		**2LiF – BeF_2**		**3LiF – AlF_3**	
Na-F	1.0(2)	Li – F	0.4(1)	Li – F	0.32(9)
K-F	0.6(2)	Be – F	24.6(8)	Al – F	13.3(8)

Because of the uncertainty in τ, discussed in 3.1.1, we treat these correlation times as qualitative measures of the relative stability of the associates.

peaked). This is also true of the K-F and Na-F FNN peaks for 2KF-NaF, although we see more pronounced peaks and therefore stronger short-range order in the case of Na-F than K-F.

The results in Fig. 1 suggest that Al-F and Be-F are distinct from the other cation–anion pairs in forming well-defined molecular associates. This interpretation is further supported by an analysis of the cage-correlation times (τ) reported in Table 2 for each of the cation–anion pairs in the three different salt solvents. The τ values for Be-F and Al-F are larger than those for all other pairs by at least an order of magnitude. The results indicate that the FNN environment for Na-F, K-F and Li-F is highly dynamic with the τ values corresponding to sub-picosecond time scales, while the Al-F and Be-F NN environments persist as stable structural entities for more than 10 ps.

The distribution of CNs for the FNN cation–anion pairs are presented in Fig. 2 in the form of the joint distributions described in Section 2.5. These distributions characterize the frequency of observing a given value of the CN and associated mean distance for the pairs in the FNN coordination shell computed for each snapshot. The results for these joint distributions were derived using the Voronoi based analysis described in Section 2.5. We note that this approach generally leads to non-integer values for the CN in a given snapshot. Also, we have found that this approach leads to averaged CNs that are smaller than those derived from Eq. 3. Thus, the results in Fig. 2 are used primarily as a way of comparing CNs across the different cation-ion pairs and salt mixtures.

In Fig. 2 the distributions for cation–anion pairs in the pure solvents (without Cr) are given in the top panels and correspond to 2KF-NaF, 2LiF–BeF_2 and 3LiF-AlF_3, from left to right (the results for systems containing Cr solute are shown in the lower three panels and are discussed in the next section). A comparison of the results across the different anion-cation pairs shows that the strongly associating cations (Be^{2+}, Al^{3+}) have comparatively lower standard deviation around their nominal CNs and around their mean separation distance (see Table S2 for values). Be^{2+} shows, as expected, a nearly unimodal distribution peaked at a value of CN near 4 with standard deviation of 0.18 as well a small secondary peak at lower CN values near 3. Al^{3+} shows CN distributions that are trimodal, with dominant peaks at CN values near 5 and 6, and a small fraction of CN near 4. This leads to a larger overall standard deviation in CN (0.48) than for Be^{2+}. The weaker associating monovalent cations (Li^+, Na^+, K^+) have CNs generally centered near 4 and with much larger standard deviation than Be^{2+} and Al^{3+}. We interpret the narrower CN distribution for Na-F relative to K-F as indicative that Na-F forms stronger short-range order than K-F, consistent with results summarized above from Fig. 1.

For the strongly associating cations (Be^{2+} and Al^{3+}) we further explore the FNN coordination using a method whereby we count the frequency of occurrence of a given number of F^- anions within the FCSR. Results are presented in Table 3, corresponding to the concentration, $\Phi_{x,z-y}$ (defined below), relative to the number of F^- ions of different $Be_xF_{z-y}^{(z-y-2x)-}$ monomers and oligomers in 2LiF – BeF_2 and $Al_xF_{z-y}^{(z-y-3x)-}$ monomers and oligomers in 3LiF – AlF_3, where x is the number of cations, z is the nominal number of F^- ions, and y is the deviation from z caused by under-coordination. These results will be discussed in detail in Section 3.1.4. Here we use these values to compute the relative frequency of observing monomer units of $BeF_{4-y}^{(2-y)-}$ and $AlF_{6-y}^{(3-y)-}$. For these monomers, y values different from zero indicate a CN different from the nominal value of 4 for Be-F and 6 for Al-F. From the numbers in Table 3 we compute that 10.0% of Be complexes are under-coordinated with CN = 3, which is not negligible. In the case of 3LiF – AlF_3, while sixfold coordination is often observed for Al^{3+}, significant fractions of 5-fold (52.3%/ monomer) and 4-fold (6.7%/ monomer) coordinated complexes are also observed. Many previous works have reported on the coordination of Al^{3+} in various molten fluorides [79,78,81,80,82], and in recent combined NMR and MD studies of $NaF-AlF_3$ and $KF-AlF_3$ a preference for CN = 5 over CN = 6 [83,84] was also reported. We note that for 2LiF – BeF_2 the previous molecular dynamics study at 700 °C using the polarized-ion model (PIM) classical force field reported that Be with CN = 3 was observed with extremely low frequency of 0.3% [30]. The origins of the discrepancies between this PIM study and the current work for the fraction of under-coordinated Be^{2+} cations are unclear, but may result from differences in the DFT methods employed here versus those used in the calculations to parameterize the PIM potential.

Finally, we have analyzed the bond-angle distributions for BeF_4^{2-} and AlF_6^{3-} associates in 2LiF – BeF_2 and 3LiF – AlF_3, respectively. The results are shown in supplemental Fig. S3, and show that the coordination environment of BeF_4^{2-} is approximately a tetrahedron with ∠ F-Be-F of 107°. Similarly, the AlF_6^{3-} associate is approximately a hexahedron with ∠ F-Al-F of 88°.

3.1.3. SNN cation-cation structures: bridging fluorides

In this subsection we consider the medium-range order characterized by the cation-cation second-nearest neighbors (SNNs), focusing specifically on the results of an analysis of common neighbor connections (CNCs), as described in Section 2.5. The presence of such medium-range order is evidenced by the peaks in the cation-cation RDFs in Fig. 1 (i.e., the SNN peaks). Examples include the small Be-Be peak in 2LiF – BeF_2 (Fig. 1)) and Al-Al peak in 3LiF – AlF_3 (Fig. 1(c)) which are indicative of SNN connections between these cations, which are mediated by their FNN coordinating F^- anions. These coordinating fluorides possess some degree of order as indicated by the F-F RDFs in Fig. 1(b) and (c). By contrast, the F-F RDF for 2KF-NaF in Fig. 1(a) is more diffuse, and the (Na-Na) and (K-K) curves are less sharp, suggesting less medium-range order.

As postulated by Baes [85], cation-fluoride associates can complex to form oligomers, linear polymers, and even cyclical structures by sharing fluoride ions. Each monomer associate consists of a cation center coordinating with fluorides. For the case of 2LiF – BeF_2 mixtures, the connection between two BeF_4^{2-} tetrahedral monomers is postulated by Baes to be achieved by either corner-sharing (sharing of one fluoride) or edge-sharing (sharing of two fluorides), and can also include the possibility of face-sharing (sharing of three fluorides). Thus, the connection motifs can either be described as different types of connection geometries

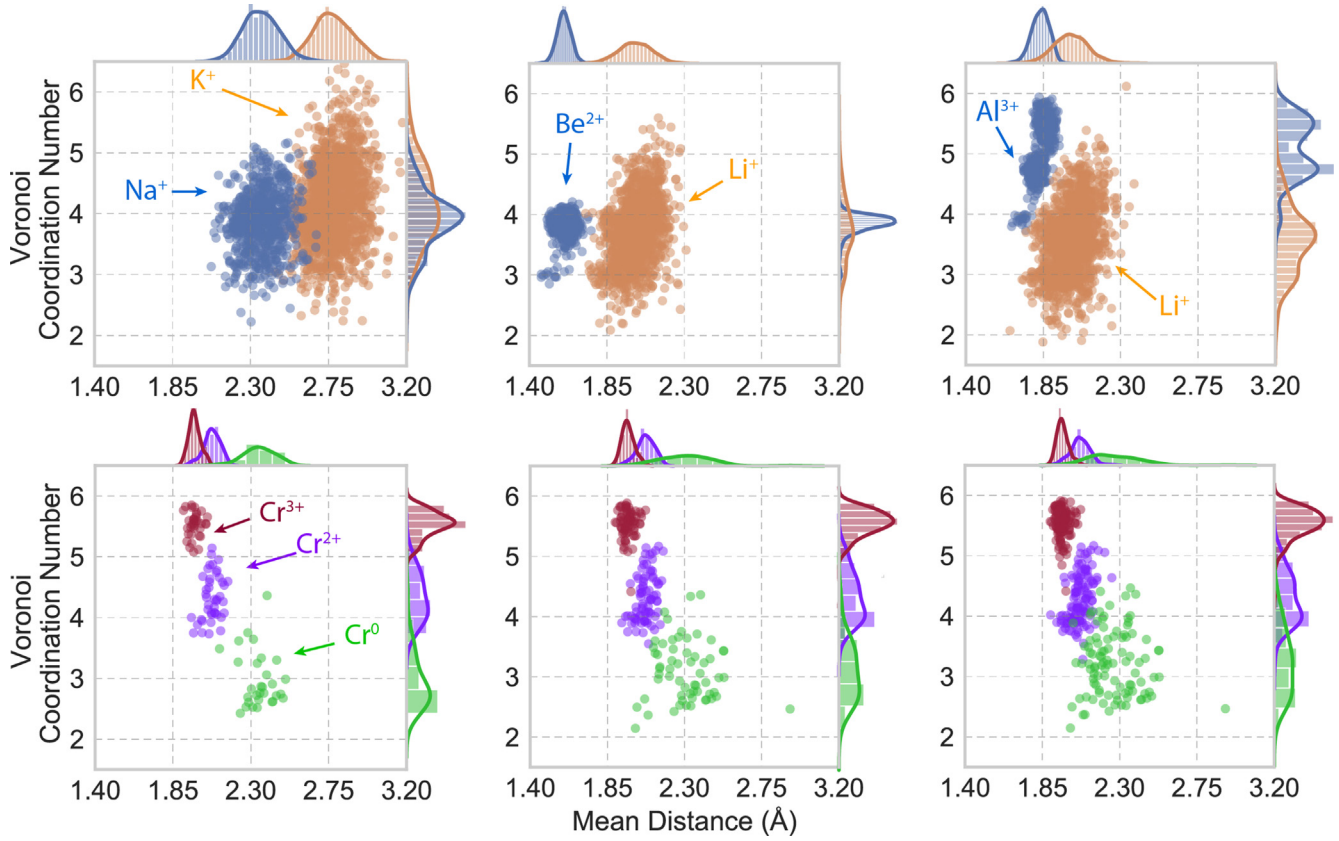

Fig. 2. CN joint distributions showing the a bi-variate scatter plot of various solute complexes existing with a given CN and mean distance (r) to its first nearest neighbor fluoride ions. Marginalized uni-variate distributions are shown for CN on the right axis and for $\bar{r}$ on the top axis. Here, CN is defined via voronoi tessellation (see Section 2).

Table 3
Fraction of monomer and oligomer species in molten $2LiF - BeF_2$ and $3LiF - AlF_3$. The values presented correspond to the mole fractions $\Phi_{x,z-y}$ defined in Eq. 7, and reported as percentages. All of the values from this work are derived from AIMD simulations at 700 °C. For $2LiF - BeF_2$, our values are compared to the thermodynamic model by Baes [85], for which the values are for 650 °C, as well as published molecular dynamics simulations at 700 °C based on the polarizable ion model (PIM) force field [70].

Fluorine Mole Fraction of Various Fluoride Oligomers					
$Be_xF_{z-y}^{(z-y-2x)-}$ in $2LiF - BeF_2$				$Al_xF_{z-y}^{(z-y-3x)-}$ in $3LiF - AlF_3$	
Species	Baes[2]	PIM	This Work	Species	This Work
F^-	15	10	13(6)	F^-	15(7)
$Be_1F_4^{2-}$, $Be_1F_3^{-1}$	54, 0	38	29(13), 5(2)	$Al_1F_6^{3-}$, $Al_1F_5^{2-}$, $Al_1F_4^{-1}$	22(10), 29(13), 4(2)
$Be_2F_7^{3-}$, $Be_2F_6^{2-}$	19, 4	19	20. (9), 3(1)	$Al_2F_{11}^{5-}$, $Al_2F_{10}^{4-}$, $Al_2F_9^{3-}$, $Al_2F_8^{2-}$	2(1), 6(3), 5(2), 0.3(2)
$Be_3F_{10}^{4-}$, $Be_3F_9^{3-}$	6, 0	10	12(5), 1.1(5)	$Al_3F_{16}^{7-}$, $Al_3F_{15}^{6-}$, $Al_3F_{14}^{5-}$, $Al_3F_{13}^{4-}$	0(0), 2.1(10), 1.5(7), 0.9(4)
$Be_4F_{13}^{5-}$, $Be_4F_{12}^{4-}$	2, 0	6	6(3), 1.7(8)	$Al_4F_{21}^{9-}$, $Al_4F_{20}^{8-}$, $Al_4F_{19}^{7-}$, $Al_4F_{18}^{6-}$	0(0), 5(2), 5(2), 0.7(3)
$Be_5F_{16}^{6-}$, $Be_5F_{15}^{5-}$	0, 0		3(1), 0.3(1)	$Al_5F_{26}^{11-}$, $Al_5F_{25}^{10-}$, $Al_5F_{24}^{9-}$, $Al_5F_{23}^{8-}$	0(0), 0(0), 0.5(2), 0.2(1)
$Be_6F_{19}^{7-}$, $Be_6F_{18}^{6-}$	0, 0	$(x > 4)$	4(2), 0.3(1)	$Al_6F_{31}^{13-}$, $Al_6F_{30}^{12-}$, $Al_6F_{29}^{11-}$, $Al_6F_{28}^{10-}$	0(0), 0(0), 0.5(2), 0(0)
$Be_7F_{22}^{8-}$, $Be_7F_{21}^{7-}$	0, 0	15	1.1(5), 0(0)	$Al_7F_{36}^{15-}$, $Al_7F_{35}^{14-}$, $Al_7F_{34}^{13-}$, $Al_7F_{33}^{12-}$	0(0), 0(0), 0(0), 0(0)
$Be_8F_{25}^{9-}$, $Be_8F_{24}^{8-}$	0, 0		0.4(2), 0(0)	$Al_8F_{41}^{17-}$, $Al_8F_{40}^{16-}$, $Al_8F_{39}^{15-}$, $Al_8F_{38}^{14-}$	0(0), 0(0), 0(0), 0(0)

1. The vertical line in column "PIM" indicates that the total fraction of oligomers with number of Be greater than 4 was determined to be 15%.
[2] In the model by Baes, y>0 values come only from corner- and edge-sharing, whereas we also consider under-coordination.

between monomer coordinates (corner, edge, or face sharing), or more generally as the number of CNCs between two SNN cations.

The results of the CNC analysis are shown in Fig. 3 for each of the cation-cation pairs across the three salt solvents. Corner sharing of the bridging fluorides (brF) is the predominant connection motif observed in both $2LiF - BeF_2$ and $3LiF - AlF_3$ (Fig. 3). CNCs between strong associates, Be-Be and Al-Al, exhibit ~100% corner sharing, while those containing weak associates, (Be, Al, Li)-Li, only posses ~80% corner sharing. By comparison, in 2KF-NaF, the proportion of 1-atom, 2-atom, and 3-atom CNCs are nearly identical for Na-Na, K-K, and K-Na, which is consistent with the overlap of SNN peaks in Fig. 1(a). These 2- and 3-atom CNCs correspond to shorter cation-cation separation compared to corner-sharing, which is to be expected geometrically. Because 2KF-NaF is only comprised of short lived associates, its CNCs can be considered as merely geometric, rather than being indicative of the formation of long-lived oligomer structures.

The CNCs have angles of 125° for Be-F-Be and 146° for Al-F-Al, as shown in Fig. S2. The dominance of corner sharing in $2LiF - BeF_2$ and $3LiF - AlF_3$ implies that oligomers of Be-F and Al-F that do not have the nominal number of fluorine atoms per cation center ($y > 0$ in Table 3) achieve this by containing under-coordinated cation centers, ucC, rather than by participating in edge- and face-sharing (CNC > 1). The thermodynamic model in Ref. [85] is built

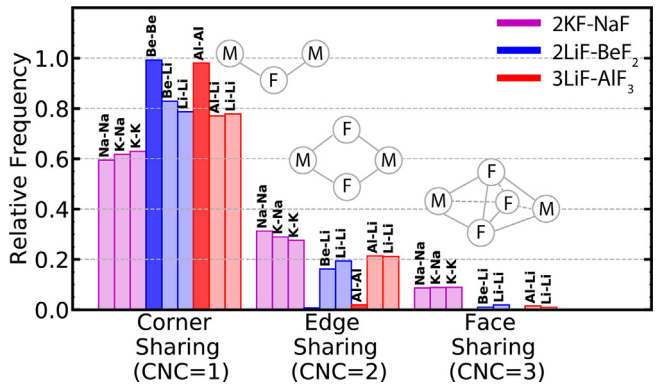

Fig. 3. Distribution of connection motifs (number of common neighbor connections, CNCs) between second nearest neighbor cations in molten fluoride mixtures. Corner sharing (1 common neighbor) is the dominant motif in all systems. 2KF-NaF is able to accommodate a larger number of 2-atom and 3-atom CNCs than $2LiF - BeF_2$ and $3LiF - AlF_3$. SNNs between cations forming strong associates (Be-Be and Al-Al) are shaded darker.

on the premise of a single type of monomer (i.e. BeF_4^{2-}), and y = 1 oligomers are assumed to form as a consequence of CNC = 2. The present results suggest that CN = 3 may need to be added as an additional degree of freedom into the thermodynamic models that fit the data for $LiF - BeF_2$ mixtures. Similarly, thermodynamic models of AlF_3 mixtures should consider monomers with CN = 6, 5, and 4.

Previous studies of $LiF - ZrF_4$ mixtures, have shown a linear relationship between MD predictions of the number of bridging fluorides, brF, and NMR F-19 chemical shift, over a range of 0.2 to 1.2 brF per monomer (i.e., per the number of strongly-associated cations, namely Be for $2LiF–BeF_2$ and Al for $3LiF-AlF_3$) [32]. This provides an experimental validation of oligomer formation. We determine the fraction of brF in $2LiF - BeF_2$ to be 0.41 brF/monomer (0.10 brF/all F). By comparison, there is less bridging, i.e., less extensive oligomer formation in $3LiF - AlF_3$, which exhibits 0.26 brF/monomer (0.04 brF/all F). For completeness, we determine 0.89 brF/ monomer (0.28 brF/all F) in 2KF-NaF; though, since this system lacks evidence for the formation of strong associates, the interpretation of these values is less straightforward.

3.1.4. Oligomer size distributions

We consider next the distribution of sizes of oligomers formed for by the relatively long-lived Be-F and Al-F associates in $2LiF - BeF_2$ and $3LiF - AlF_3$. Our principle point of comparison for these distributions is the work of Baes [85]. In that work, a thermodynamic model for $LiF - BeF_2$ melts was proposed, which was based on a polymer model for silicates. It describes the melt as a mixture of ionic oligomers with varying lengths and connection motifs, and was fit using available thermodynamic data for $LiF - BeF_2$ mixtures. From this fit, the oligomer concentrations are expressed in terms of the fraction of fluorine atoms contained within each type of oligomer:

$$\Phi_{x,z-y} = \frac{(z-y)n_{x,z-y}}{N_{F^-}} \tag{7}$$

where $n_{x,z-y}$ is the number of moles of species with x cations (Be or Al) and $z - y$ fluoride anions, with y specifying under-coordination from the nominal value of z (namely $4x$ for Be-F and $6x$ for Al-F), and N_{F^-} the total moles of F^- in the melt.

We calculate these mole fractions $\Phi_{x,z-y}$ from the present simulations and present the results in Table 3, which also includes a comparison to the results from the thermodynamic model of Baes [85] and previous simulations based on the PIM force field [30]. The present results are seen to agree with the previous PIM simulations to within a few percent. Comparing to the Baes model [85], the current results indicate less dissociated F, dsF, by 0.15, fewer monomers by 0.40, and oligomers as long as x = 8. Longer oligomers are of decreasing predominance, with two probability jumps for Be_6F_{19} and Be_4F_{12}. A similar probability jump is observed for Al_4F_{19} and Al_4F_{20}.

If we naively repeat the same oligomer analysis as used for $2LiF - BeF_2$ and $3LiF - AlF_3$ above, also for the case of 2KF-NaF, we calculate a dissociated F^- volume fraction of 0.20 (0.6 dsF/-monomer). As discussed in [86], however, for RDFs that do not drop to zero beyond the first peak, the first coordination shell and the maximum bond length are not equivalent. To partially remedy this, we fit a Gaussian distribution to the first Na-F peak and define the cutoff radius as the point at which the Gaussian decays below 0.05 (which corresponds to 2.55Å versus the FCSR value of 2.74Å). With this definition, we calculate a dissociated F^- mole fraction of 0.31 (0.93 dsF/monomer). This might be in line with the notion that 2KF-NaF is the most fluorobasic of the three melts, though it does clash with the picture of 2KF-NaF as being "completely" dissociated. We do note that in this analysis, the remaining 0.70 volume fraction is comprised of a large variety of very long Na-F networks containing anywhere from 2 to 16 Na atoms, the latter of which corresponds to all Na atoms in our simulation cells. As discussed in Section 3.1.2, however, Li-F, K-F and Na-F have characteristic cage correlation times of less than 1 ps, and we thus believe it is sufficient to consider these as dissociated ions with geometrically-defined connectivity; if we were to incorporate a notion of time-stability, these networks would be highly dynamic and disappear on very short time scales. Going forward, in the discussion of Cr solvation, we will only consider the oligomer picture further in the analysis of the salt mixtures containing Be-F and Al-F associates.

3.2. Incorporation of Cr into solvent structure

In this section we consider the solvation structure of Cr solute in the three salt mixtures. The solvent structure is considered for three charge states, namely Cr^0, Cr^{2+} and Cr^{3+}. We characterize this structure in terms of the FNN coordination numbers, second-neighbor connection motifs, and oligomer structures in the subsections that follow. We also discuss the ways in which the presence of Cr solute changes the structure of the solvent.

3.2.1. FNN solute-anion coordination

We start with an analysis of the FNN CNs between Cr^{x+} solutes and F^- anions, based on the results for the joint distributions presented in the bottom row of Fig. 2. The average values and standard deviations for the CNs and bond lengths derived from these distributions are presented in Table S2. The results show two main trends. First, there is a tendency for the CN to increase and the bond-length to decrease as the oxidation state of Cr^{x+} increases from x = 0 to 2 to 3, and this trend is the same for all three solvent salt mixtures. Second, the preference for a given coordination environment, as measured by the standard deviations of the distributions for bond length and CN, is strongest (i.e., characterized by smallest standard deviations) for Cr^{3+} and weakest (i.e., largest standard deviations) for Cr^0, with the behavior of Cr^{2+} being intermediate. The FNN CNs for Cr^{3+} are peaked at values near 6 in Fig. 2 for all three solvent salt mixtures. For Cr^{2+}, the distributions are relatively wider, centered on CN values near 4, with some sampling of CN values near 5. The neutral Cr^0 solute species samples CN values spanning 2 to 4; they have a relatively wide range of FNN Cr^0-F^- bond lengths, in a manner similar to the distributions for Li^+-F^-, K^+-F^- and Na^+-F^- in the pure solvent mixtures discussed above.

The results from the joint distributions presented in Fig. 2 and Table S2 suggest that Cr^{3+} forms the strongest associates with F^-, with CN environments that vary relatively little across the three solvent salt mixtures. By contrast, Cr^0 shows less evidence for the formation of strong associates with F^-, and the behavior of Cr^{2+} is intermediate between the two. These tendencies related to Cr^{x+}-F^- associate formation for Cr^{x+} in different oxidation states can be further analyzed using the results for cage-correlation times in Table 4. The largest values for τ are found for Cr^{3+}-F^-, consistent with the interpretation that they form the strongest associates. The Cr^{3+}-F^- correlation times are in fact longer than those obtained for the Al^{3+}-F^- and Be^{2+}-F^- associates discussed in the previous section (see Table 2). The values of τ are roughly an order of magnitude smaller for Cr^0-F^- relative to Cr^{3+}-F^-, and are several times smaller than the values for Al^{3+}-F^- and Be^{2+}-F^- in Table 2, consistent with the interpretation that Cr^0-F^- does not show evidence of forming strong associates. The correlation times for Cr^{2+}-F^- are slightly larger than for Cr^0-F^- but significantly smaller than for Al^{3+}-F^-, Be^{2+}-F^-, and Cr^{3+}-F^- associates.

To examine the effect of Cr solvation on the cage correlation time for the solvent cations, values for τ are given for all cation–anion pairs in the pure salt mixtues and systems containing Cr in Table S1. We note that solvation of Cr^{2+} leads to an increase in τ for Be^{2+}-F^- (from 24 to 28 ps) and Al^{3+}-F^- (from 13 to 25 ps). Similarly, solvation of Cr^{3+} leads to an increase in τ for Be^{2+}-F^- (to 27 ps), and Cr^0 to a decrease in τ for Be^{2+}-F^- (to 18 ps).

Overall, the results presented in this subsection indicate a correlation between higher charge states and stronger associates for Cr solutes with F^-, as indicated by the increasingly peaked nature of the joint distributions with increasing oxidation state and the longer cage-correlation times.

3.2.2. SNN solute-cation structures

We consider next the connection motifs between Cr solutes and SNN cations, employing the CNC analysis presented in Section 3.1.3. Fig. 4 shows results for CNCs between Cr solute and solvent cations, which are qualitatively similar to those presented in Fig. 3 for cation-cation SNNs in the pure solvent salt mixtures. Specifically, Be-Cr and Be-Be SNNs both possess ~100% corner sharing CNCs, and Cr-Na, Na-Na, Cr-K, and K-K all possess ~60% corner sharing CNCs. Al-Cr SNNs show predominantly corner sharing CNCs, but the fraction is slightly reduced compared to Al-Al. Cr-Li shows ~70% corner sharing in both $2LiF–BeF_2$ and $3LiF-AlF_3$. Interestingly, these results for solute-cation SNNs are largely independent of Cr oxidation state.

We further examine the SNN connection motifs by calculating the number of bridging fluorides (brF) before and after Cr addition in the associate-forming $2LiF–BeF_2$ and $3LiF-AlF_3$ salts. For both solvents we observe a slight change of brF upon Cr addition. In $2LiF-BeF_2$, upon addition of both Cr^{2+} and Cr^{3+}, we see the brF fraction changes from 0.41 brF/monomer to 0.35 brF/monomer and 0.39 brF/monomer, respectively. In $3LiF-AlF_3$, after adding Cr, the fraction changes from 0.26 brF/monomer to 0.36 brF/monomer for Cr^{2+}, and to 0.43 brF/monomer for Cr^{3+}. We return to the analysis of these bridging anions in the discussion of oligomer structures in the next subsection.

Additional insight into the nature of the cation-cation connection motifs is obtained by considering results for $g^{\gamma}_{\alpha\beta}(r)$, i.e., the CNC-based decomposition of the cation-cation RDFs. Fig. 5 shows results of this analysis for the cases of the $2LiF-BeF_2$ and $3LiF-AlF_3$ salt mixtures, both with and without the addition of Cr solute species in different oxidation states. In the analysis, we define all CNCs within a given oligomer as "intra-oligomer" connections, to distinguish them from "inter-oligomer" connections between different (disconnected) oligomers (see Fig. 6 for an illustration). For a visual representation of the different types of intra-oligomer connections observed in simulation snapshots, the reader is referred to Figs. S4 and S5.

We focus first on Fig. 5 (a) and (e), showing $g^{\gamma}_{\alpha\beta}(r)$ for Be-Be and Al-Al SNNs in pure $2LiF–BeF_2$ and $3LiF-AlF_3$, respectively. For both systems we see that the intra-oligomer peaks are present at smal-

Table 4
Characteristic cage-correlation times (in ps) for Cr-F NN pairs in the different solvents and for different Cr oxidation states, obtained by by fitting τ in Eq. 6. Results can be compared to those for cation-F pairs in the pure solvents in Table 2.

	2KF – NaF	2LiF – BeF_2	3LiF – AlF_3
Cr^0	4(1)	2.3(7)	6(1)
Cr^{2+}	9(2)	6(2)	7(2)
Cr^{3+}	159(93)	67(16)	26(4)

Because of the uncertainty in τ, discussed in Section 3.1.1, we treat these correlation times as qualitative measures of the relative stability of the associates.

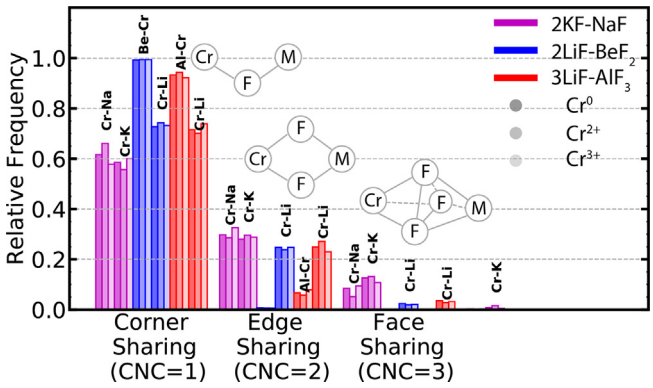

Fig. 4. Distribution of connection motifs (number of common neighbor connections, CNCs) of second nearest neighbors for Cr-M pairs (where M = Al, Be, K, Li and Na is a cation in the solvent host). Similar distributions are observedthe solvent counter-parts of the Cr-M pairs (Fig. 3) and differences are small across the different charge states or Cr.

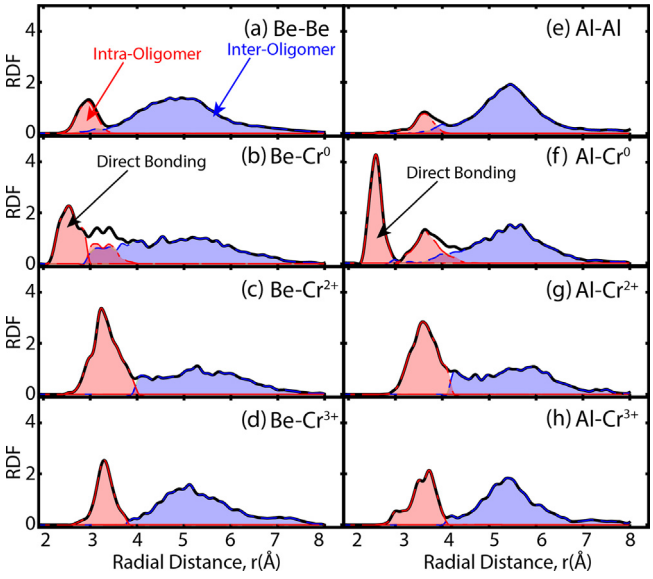

Fig. 5. Radial distribution function for Be-Be, Be-Cr, Al-Al, and Al-Cr pairs decomposed according to connections happening within a single oligomer (intra-oligomer) and between different oligomers (inter-oligomer). (a) and (e) show this for Be-Be in pure $2LiF–BeF_2$ and Al-Al in pure $3LiF-AlF_3$. (b)/(f), (c)/(g), and (d)(h) show this for Cr^0, Cr^{2+}, and Cr^{3+}, respectively, in $2LiF–BeF_2$/$3LiF-AlF_3$.

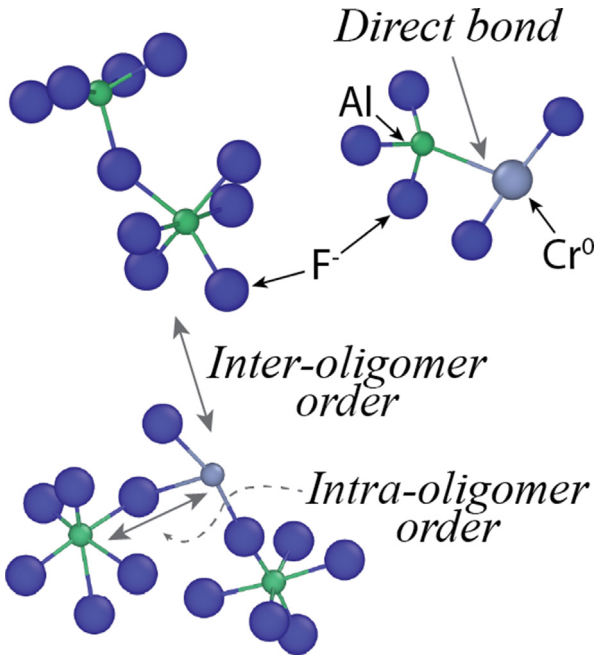

Fig. 6. Illustration of the inter-oligomer and intra-oligomer cation-cation neighbors.

ler bond lengths, centered at approximately 3.0Å and 3.5Å for 2LiF–BeF_2 and 3LiF-AlF_3, respectively. The inter-oligomer pairs are in both cases characterized by broader distributions centered at larger neighbor spacings. Turning to Figs. 5 for SNNs involving Cr^{2+} and Cr^{3+}, we see that the $g^{\gamma}_{\alpha\beta}(r)$ contain non-zero values only for Cr-Be and Cr-Al distances beyond approximately 2.8Å and 3.0Å, respectively. The first peaks beyond these distances are composed entirely of solute-cation SNNs that are intra-oligomer, i.e., corresponding in (c) and (d) to Cr-F and Be-F associates sharing common F^- ions, and similarly for (g) and (h) for Cr-F and Al-F associates. These peaks are more prominent than for the Be-Be or Al-Al intra-oligomer cases in the pure salt mixtures, indicative of increased oligomer size upon addition of Cr.

In comparison to the cases for Cr^{2+} and Cr^{3+} solutes, the $g^{\gamma}_{\alpha\beta}(r)$ distributions for the case of Cr^0 shown in Figs. 5(b) and (f) each display an additional feature. Specifically, we see in both cases the presence of sharp peaks at distances shorter than those for the intra-oligomer neighbors between Cr^{2+} or Cr^{3+} solutes and host cations. While these peaks correspond to intra-oligomer cation-cation neighbors, these neighbors involve much shorter bondlengths that are in fact comparable to those found between Cr and Al or Be nearest neighbor bonds in the stable intermetallic compounds present in the Cr-Be and Cr-Al phase diagrams [87,88]. Further, we have found that the Cr^0-Be^{2+} and Cr^0-Al^{3+} neighbors with these short bondlengths have very long correlation times, that are significant fractions of the total simulation times. We interpret these characteristics of short bondlengths and long correlation times as reflecting *direct* bonding between Cr^0 and solvent Be^{2+} or Al^{3+} cations. Representative simulation snapshots illustrating oligomers including these Cr^0-Be^{2+} and Cr^0-Al^{3+} direct bonds are found in Figs. S4 (b) and S5 (b), respectively. These snapshots can be contrasted with those in Figs. S4 (a) and S5 (a), where the intra-oligomer Cr^0-Be^{2+} and Cr^0-Al^{3+} neighbors involve intermediate bridging F^- anions, and feature longer bondlengths. We return to the possible significance of this surprising evidence of "direct" bonding between Cr^0 and host solvent cations in Section 4.

3.2.3. Oligomer size distributions

Table 5 tabulates data that characterizes the solvation structure of Cr in relation to the oligomer distributions in the associate-forming 2LiF–BeF_2 and 3LiF-AlF_3 salt mixtures. For each mixture, the first row presents data for the pure salt, followed by results for systems containing Cr^{x+} solutes in each of the oxidation states x = 0, 2, 3. The results thus enable characterization of the solvation structure as well as the Cr-induced changes to the oligomer structure for the solvent salt mixtures. Fig. 7 illustrates the meaning of some of the key quantities listed in Table 5, and defined in further detail below. We note that to facilitate the comparison of statistically-significant changes between the pure salt-mixtures and those with Cr solutes, we include in Table 5 estimates of the statistical uncertainties from the simulation data.

In Table 5, Cr-containing oligomers are referred to as Cr-COs. The entries dsF, brF, and ucC are as defined before for the Be-F and Al-F networks and are always normalized to N_M, the monomer count (i.e., the number of Be or Al cations). Here, the negative values for dsF in Cr-COs represent the F^- anions that are uniquely associated with Cr, and are otherwise counted as dsF in the Be-F and Al-F oligomer network. Additionally, brF in Cr-COs are defined as before, and represent the bridging F^- anions of strong associates: Be-F-Be and Al-F-Al. ucC are also defined as before, representing CN<4 for Be-F and CN<6 for Al-F. The average number of SNNs that a Cr solute ion possesses is referred to as Cr SNN. A SNN count of one would indicate a terminal position in the oligomer, a value of two would indicate that Cr is located within a linear oligomer, and a value greater than two would indicate that Cr is a branching point. To aid in visualization of these different situations, the reader is referred to the snapshots of Cr-COs from our simulations, which we believe to be representative, in Figs. S4 and S5. The average oligomer sizes in Table 5 are reported for solvent and solvent + solute oligomers; solvent oligomers include (Be,Al)-F connections; solvent + solute oligomers are the Cr-COs and they include (Be,Al)-F, Cr-F, and Cr-(Al,Be) connections.

The solutes mainly appear to be incorporating in the oligomer network by bridging two solvent oligomers, as evidenced by the fact that the length of the Cr-COs is roughly twice that of the Be-F and Al-F oligomers. For example, Cr^0-COs in 2LiF–BeF2 are 5.3 in length; subtracting the Cr monomer, and dividing by two, we obtain 2.2(7), which is equal to the 2.1(2) average length of the Be-F oligomers within statistical error bars. Within 95% confidence, this is true for all of the three valence states of Cr in both 2LiF–BeF_2 and 3LiF-AlF_3. The average length of the solvent oligomers does not change appreciably with addition of the Cr solutes; the one exception is the extension of the Al-F average oligomer length from 1.70 (13) to 2.4(3) upon addition of Cr^0. All Cr SNN coordinations are close to the value of 2, further supporting the hypothesis of Cr solutes incorporating inside of solvent oligomers. SNNs for Cr^0 and Cr^{2+} in 2LiF–BeF2 are within one standard error of the value of 3, thus showing evidence of oligomer branching at the Cr^0 and Cr^{2+} solutes.

The fraction of Cr observed as single Cr-F monomers is the lowest for Cr^0 and increases for Cr^{2+} and even more so for Cr^{3+}; the fraction is always lower in 2LiF–BeF_2 than in the 3LiF-AlF_3 solvent. If the solvation of Cr were were fully explained by associating the dsF with the Cr solutes, with otherwise no change in the (Al,Be)-F network in the solvent, then we would expect a reduction of dsF upon addition of Cr, and appearance of the corresponding number of single Cr-F monomers. Considering the respective CNs of Cr in the two solvents, the decrease would be in the range of 0.17 to 0.58 dsF. Based on the dsF standard errors in Table 5, these would be statistically significant changes. For Cr^0, no such difference in dsF appears in either solvent. For Cr^{2+} and Cr^{3+}, a decrease in dsF is observed.

Table 5
Summary of dsF, brF, and ucC with and without added Cr in strongly associated solvents. The numbers in parentheses represent the standard error for the last significant figure.

Solvent	Solute	Oligomer Type [1]	$\frac{dsF}{N_M}$	$\frac{brF}{N_M}$	$\frac{ucC}{N_M}$	Cr SNNs [4]	Oligomer Size
2LiF-BeF_2	N/A	Be-F	0.51(4)	0.42(3)	0.100(5)		2.4(2)
	Cr^0	Be-F	0.57(8)	0.37(5)	0.20(4)		2.1(2)
		Cr-Be-F	0.00(4)			2.5(7)	5(1)
	Cr^{2+}	Be-F	0.47(3)	0.34(3)	0.12(1)		2.0(2)
		Cr-Be-F	−0.13(4)			2.5(4)	5.1(9)
	Cr^{3+}	Be-F	0.51(2)	0.39(3)	0.12(2)		2.2(2)
		Cr-Be-F	−0.29(3)			1.8(4)	5(1)
3LiF-AlF_3	N/A	Al-F	0.91(5)	0.26(4)	0.59(3)		1.7(1)
	Cr^0	Al-F	1.0(1)	0.39(5)	0.62(3)		2.4(3)
		Cr-Al-F	−0.13(4)			2.3(4)	5(1)
	Cr^{2+}	Al-F	0.69(2)	0.21(2)	0.47(2)		1.50(7)
		Cr-Al-F	−0.21(5)			1.9(5)	3.3(7)
	Cr^{3+}	Al-F	0.86(2)	0.31(3)	0.55(3)		1.8(1)
		Cr-Al-F	−0.42(4)			1.7(4)	3.6(8)

[1] Whether statistics should be gotten for the host oligomers (Be-F or Al-F), or for the Cr-CO.
[2] $\frac{1}{N_M}$ refers to normalization by number of strong associate monomers: Be in 2LiF–BeF_2 and Al in 3LiF-AlF_3
[3] dsF in the rows "Cr-Be-F" and "Cr-Al-F" refers to the impact on the host dsF. It indicates the F fraction that is bound only to Cr and not Be or Al, and therefore a negative value indicates "taking" F from the host.
[4] ucC are cations whose CN is less than 4 for Be and 6 for Al. In counting ucC, we weight by the deviation from these values, e.g. CN = 2 is counted twice for ucC of Be.
[e5] SNN specifically refers to the number of brF that connect to a central Cr (see text for discussion), and "Oligomer Size" refers to the average oligomer size.
[f6] In the simulation cell, Cr:Be = 1:14 and Cr:Al = 1:10.

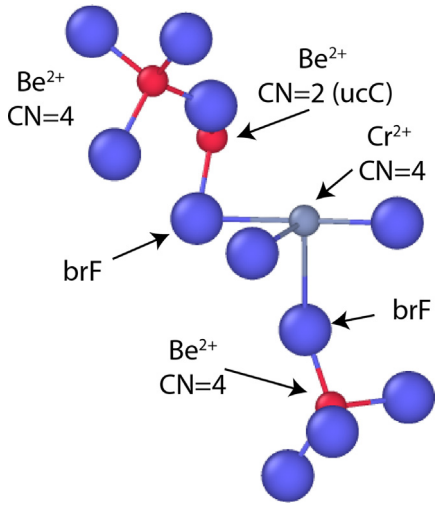

Fig. 7. Illustration of a Cr-containing oligomer (Cr-CO), defining the meaning of the brF and ucC quantities referred to in Table 5.

Considering only the Al-F associations (and not the Cr-F associations) a unique observation is made for the Cr^{2+} solute in 3LiF-AlF_3: dsF decreases from 0.91(5) to 0.69(2). This indicates a modification in the Al-F oligomer network where dsF either reacts with brF (decreasing the length of the Al-F oligomers) or decreases ucC (increasing the CN of Al-F). The other sources for the F coordinating with Cr could be either through brF or ucC. The only statistically significant increase of brF is with Cr^0 addition to 3LiF-AlF_3; the standard error is sufficiently small relative to the number of F^- ions that coordinate with Cr to not overshadow such changes in brF in the other solute–solvent combinations. Thus, the presence of Cr^0 in 3LiF-AlF_3 uniquely increases the incorporation of F anions into the oligomer network of Al-F.

In 2LiF–BeF_2, ucC remain essentially unchanged by the addition of Cr^{2+} and Cr^{3+} solutes; the standard error is sufficiently small relative to the number of F anions that coordination with Cr does not overshadow such changes in ucC. ucC significantly increases for the Cr^0 solute from 0.10(5) to 0.17(3); thus, a higher prevalence of BeF_3^- is observed upon addition of Cr^0, and even a small appearance of BeF_2. In 3LiF-AlF_3, ucC decreases for all Cr in all valence states, and thus a higher prevalence of AlF_6^{3-} is observed, or a lower prevalence of AlF_4^-.

Overall, none of the changes in dsF, brF, and ucC account for the observed CNs for Cr. This is further evidence for the observation made earlier that Cr solvates by incorporation within the oligomer network of the solute. Otherwise stated, the F anions that are part of coordinating and solvating Cr solutes also remain associated with the solvent cations. This suggests a picture of the Cr being solvated partly by the solute oligomers and partly by dsF; for Cr^0 and Cr^{2+}, the role of dsF solvation relative to oligomer solvation is statistically insignificant; for Cr^{3+}, dsF solvation dominates over the oligomer solvation mode, at a relative amount of 70(30)% in 2LiF–BeF_2 and 70(20)% in 3LiF-AlF_3.

4. Discussion

4.1. Solvent fluoroacidity

Fluoroacidity of a melt, or a_{F^-}, is related to the concentration of dsF (often termed "free" fluorides) [24,22]. The present study investigates not only the concentration of dsF, but also the acidic species that are in equilibrium with dsF. These acid-base reaction equilibria ultimately dictate the a_{F^-} of the melt, which in turn depends on both concentration and activity coefficients of dsF.

The first metric to be considered in assessing the fluoroacidity of a solvent is the formation of weak and strong associates between the cations and F^-. In this context, K^+, Na^+ and Li^+ cations are highly fluorobasic because they do not form strong associates. The standard deviations of the Na-F coordination are not as broad as in the case of K-F, thus the Na^+ cation can be classified as somewhat less fluorobasic than K^+. These observations are in-line with observations by [89,90]. Similarly, Be^{2+} and Al^{3+} form strong associates and we can conclude that they are both more fluoroacidic than Li^+, in line with prior observations by [89,90].

We further consider acid-base behavior in fluoride melts that contain cations forming strong associates. The variability in the CNs of the monomers and the formation of oligomers demonstrate that there are two types of acid-base reactions that occur within such melts: that of a change in monomer CN and that of association-dissociation of oligomers. Taking as a specific example the case of 2LiF–BeF_2:

Increase in Be-F coordination number:
$BeF_3^- + F^- \leftrightarrow BeF_4^{2-}$.
similarly, $Be_2F_6^{2-} + F^- \leftrightarrow Be_2F_7^{3-}$.
and generally, ucC(acid) + F^-(base) ↔ fully coordinated cation
Dissociation of oligomers:
$Be_2F_7^{3-} + F^- \leftrightarrow 2BeF_4^{2-}$.
and generally, brF(acid) + F^-(base) ↔ 2 terminal F^-

where ucC are under-coordinated cations and brF are bridging fluorides.

The acidic species in the melt are the oligomers, quantified by brF, and the under-coordinated complexes, quantified by ucC. The number of bridging fluorides can thus be one metric for the acidity of a melt, experimentally measurable by liquid NMR [32,96,97]. This would need to be paired with information about the distribution of coordination numbers for the monomers, measurable by X-ray or neutron diffraction [71]; identification of ucC, as well as salt dimers, has also been demonstrated to be possible using Raman spectroscopy [91,31,78,79].

In the present study the $2LiF - BeF_2$ and $3LiF - AlF_3$ compositions were chosen to match the stoichiometry of fully coordinated Be-F and Al-F. Neither of the melts demonstrate a zero concentration of dsF, which indicates an important contribution from ucC and brF acidic species. In $2LiF - BeF_2$, the contribution to acidity comes dominantly from oligomers, with 0.42(3) brF/monomer, and secondly from CN = 3 monomers, which lead to 0.100(5) ucC/-monomer. In $3LiF - AlF_3$, the contribution to acidity comes dominantly from ucC (CN = 5 and CN = 4 monomers) with 0.59(3) ucC/monomer, and secondly from oligomers, with 0.26(4) brF/-monomer. This approach to definition of acidity is similar to that described by [92], where basicity is described as a tendency to liberate F-. Based on this metric of acidity, (brF + ucC) per strongly-associating cation (i.e., per monomer), it would be concluded that the overall fluoroacidity of AlF_3 in $3LiF - AlF_3$ is higher than that of BeF_2 in $2LiF - BeF_2$. This concept is subsequently discussed in 4.2 in the context of acid-base buffering capacity.

If instead, qualitative fluorobasicity comparisons were to be made on the basis of dissociated F^- concentration (dsF), then the opposite would be concluded: dsF/monomer = 0.51(4) for $2LiF - BeF_2$ and 0.91(5) for $3LiF - AlF_3$. Hence one might conclude that AlF_3 is more basic than BeF_2. Neither of these approaches capture the effects of activity coefficients, which would be needed for a correct prediction of fluoroacidity. Fig. 8 shows a summary of the interdependence of the solvent structure features discussed here.

4.2. Cr solvation

The conceptual framework previously used in the literature to consider Cr solvation is based on a simplified concept of fluoroacidity. If Cr is to become solvated in the melt, it must either capture dsF or take F^- from existing coordination complexes in the melt. A high a_{F^-} reduces the need to compete for F^- and makes solvation of the higher valence state more favorable in fluorobasic melts than in the fluoroacidic ones [24]. This framework has been used to argue why the highly fluorobasic LiF-NaF-KF mixture is more corrosive than $2LiF - BeF_2$; however evidence of very highly acidic melts having unfavorable corrosion behavior has also been reported [22]. A fundamental explanation for the latter has yet to have been proposed and is addressed by the results presented here. 2KF-NaF forms no strong, long-lived, associates, such that all of its anions are essentially dsF. When Cr solutes are added, time-stable

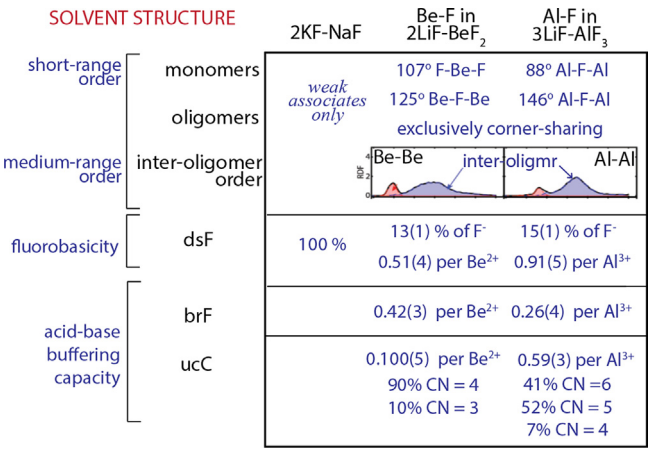

Fig. 8. Summary description of solvent structure.

associates form, with CrF_6^{3-} having cage-correlation time of 160 (90) ps and that of CrF_4^{2-} being 9.1(1.6) ps. In the case of $2LiF–BeF_2$, there are 7.1(6) dsF/Cr available. Upon addition of the Cr solutes, there is no statistically-significant change in dsF (see Table 5) and $Cr^{2+/3+}$ still attain their nominal CNs; their cage correlation times and Cr-F bond-lengths are, within the uncertainties, similar to those of the Cr-F complexes that form in 2KF-NaF (Table S2). This observation challenges the previous concept of Cr solvation by dsF.

We observe that 1.8(6) dsF/Cr associate with Cr^{2+}-F monomers and 4.1(4) dsF/Cr associate with Cr^{3+}-F monomers. The remaining fluorides needed to achieve the nominal CNs for Cr^{2+} and Cr^{3+} are attained by integration into the Be-F oligomer network, where Cr solvation involves brF. This pattern repeats in the case of $3LiF-AlF_3$, where there are 9.1(5) dsF/Cr available, which does not change by a statistically-significant amount upon addition of Cr, either. Nevertheless, Cr^{2+} and Cr^{3+} still attain their nominal CNs, and the Cr-F cage correlation times and bond-lengths are similar to those in 2KF-NaF and $2LiF–BeF_2$.

These observations suggest a combination of two solvation effects that relate to fluoroacidity. First is solvation by dsF leading to formation of Cr-F monomers; fluorobasic melts would have a higher concentration of dsF. Second is solvation by oligomers leading to incorporation of Cr in the oligomer network of the solvent; fluoroacidic melts would have a higher propensity for oligomer solvation. Taking the specific example of Cr^{2+} (CN = 4) solvation in $2LiF–BeF_2$:

Solvation by dsF:
$CrF_3^- + F^- \leftrightarrow CrF_4^{2-}$.
similarly, $CrBeF_6^{-2} + F^- \leftrightarrow CrBeF_7^{-3}$.
and generally, ucCr(acid) + F^-(base) ↔ fully coordinated Cr
Solvation by oligomers:
$CrF_2 + 2Be_2F_7^{-3} \leftrightarrow CrBe_4F_{16}^{-6}$.
and generally, ucCr (acid) + oligomers ↔ longer oligomer

As reported in Section 3.1.4, for Cr^{3+}, dsF solvation dominates over the oligomer solvation mode (70(30)% in 2LiF–BeF2 and 70 (20)% in 3LiF-AlF3), whereas for Cr^{2+} both mechanisms of solvation are equally significant. These results indicate that higher CN solutes are incorporated into the oligomer network to a lesser extent. We hypothesize that steric effects may be present for oligomer solvation of solutes that have higher-CNs and lower Cr-F bond

length, as is the case for Cr^{3+} vs Cr^{2+}. As noted in Section 3.1.4, solute SSNs show that Cr^{2+} is more likely than Cr^{3+} to be an oligomer branching point.

Both of these pictures, of solvation by dsF and by oligomers, are complicated by the production of new dsF via the two routes discussed in Section 4.1, namely the increase in either ucC or brF. At one extreme, melts that consist of strong associates but no oligomers (brF = 0, only monomers) and a unique solvent cation CN (no possibility for ucC >0) would not have the capability to produce dsF in response to the consumption of a dsF by solvation of a Cr cation. Such melts would have no *acid-base buffering capacity*. Conversely, melts with a high brF concentration or with a capacity for under-coordination (multiple possible CNs, as in the case of Al-F) *would* have acid-base buffering capacity. Our results indicate that both $2LiF-BeF_2$ and $3LiF-AlF_3$ have buffering capacity, as discussed above in Sections 4.1 and 3.1.4.

Lastly, we note that Cr^0 is unique and does not form lone monomers. Thus the more acidic melts are expected to facilitate solvation of Cr^0. The possible CNs of Cr^0 are 2, 3 and 4 and are attained by oligomer solvation and by direct bonding.

It is unknown if there is a relationship between direct bonding and acidity. From the present results, we observe evidence for direct bonding of Cr^0 only with the cations that form strong associates with F^-. While there might be a trend in increased direct bonding with increased melt acidity, the relationship between Cr^0 direct bonding and melt acidity merits further investigation. The role of solvated Cr^0 in corrosion mechanisms has not yet been explored, and also merits future investigation. For example, dissolution followed by electron exchange in the melt can be considered as an alternative mechanism to the assumed electron exchange at the metal surface followed by dissolution of the corrosion product cation.

Fig. 9 shows a summary of the interdependence of the chromium solvation and solvent structure features discussed here. In light of the analysis above, it is interesting to consider the results of [24], which show that the Cr^{3+}/Cr^{2+} concentration ratio increases in $LiF-BeF_2$ mixtures as the ratio $LiF:BeF_2$ is increased above 2:1. The authors' claim that dsF = 0 in $2LiF-BeF_2$ is not supported by our results; rather, the observations can be understood if one considers that the higher F/Be ratio upon addition of LiF can lead to lower ucC, higher dsF, or possibly lower brF, all of which can facilitate the solvation of higher CN-number Cr^{3+} over the lower CN-number Cr^{2+}. The effect of fluoroacidity on the equilibrium concentration of oxidized Cr in the melt was also studied in [93] and discussed in [22], which indicate that both extremely basic melts and highly acidic melts will lead to the a higher equilibrium concentration of dissolved chromium ions. The lowest equilibrium concentration was observed at a melt that is somewhere in-between very acidic and very basic. By contrast, Duffy shows a monotonic, linear dependence of Fe^{2+}/Fe^{3+} with optical basicity (measured by red-shift in UV–vis) in molten silicate glasses [92]. These previous results, taken alongside our current results, show that, while basicity may correlate with stabilizing higher valance cations, there is a more complex interplay of brF, dsF, and ucC that underpins this simple metric.

5. Summary and conclusions

Ab-initio molecular dynamics (AIMD) simulations were undertaken to examine the solvation of Cr in fluoride molten-salt mixtures with varying chemistry and solute oxidation state. Simulations were undertaken at 700°C for 2KF-NaF, $2LiF-BeF_2$ and $3LiF-AlF_3$ solvent salt mixtures, considering Cr^{+x} solute with x = 0, 2, and 3. The short- and medium-range order of these systems was analyzed considering radial distribution functions,

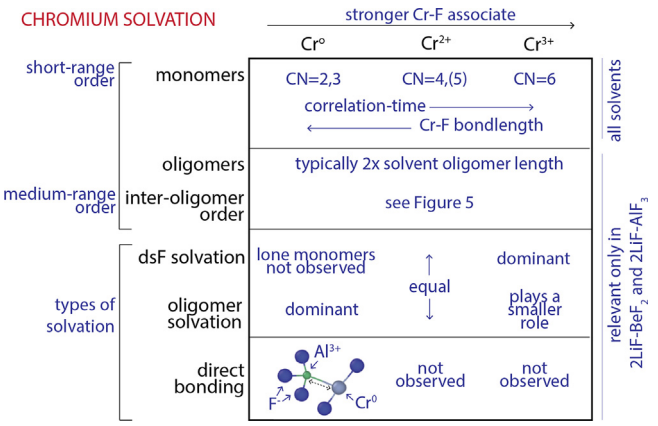

Fig. 9. Summary description of chromium solvation.

cage-correlation times, common-neighbor connections, and oligomer size distributions. The analyses were used to determine characteristic features of Cr solvation structures, and to probe solute effects on the structure of the solvent host. The results were compared to traditional pictures of solvation based on the concept of fluoroacidity.

For the pure solvent salt mixtures, the 2KF-NaF system is characterized by a highly dynamic structure where the cation-fluoride FNNs form local order that changes on sub-ps timescales. By contrast, in $2LiF-BeF_2$ and $3LiF-AlF_3$, Be-F and Al-F form long-lived associates that are connected in well-defined oligomer structures. The simulations predict appreciable concentrations of associates that are under-coordinated relative to the nominal CN values of 4 for Be-F and 6 for Al-F: approximately 10% of the Be-F associates were found to be BeF_3^-, and the majority of the Al-F associates (approximately 52%) were AlF_5^{2-}. For both $2LiF-BeF_2$ and $3LiF-AlF_3$, oligomers were formed through corner-shared bridging fluoride ions, with average lengths of 2.4 monomers for Be-F oligomers and 1.7 monomers for Al-F oligomers.

Cr solutes in these salt mixtures were found to display a distribution of CNs centered near 6 for Cr^{3+}, near 4 for Cr^{2+}, and spanning a range of values between 2 to 4 for Cr^0. The average bondlengths in the solvation shells were found to decrease with increasing oxidation state. Further, the preference for a given coordination environment, as characterized by the standard deviations of the CN and bondlength distributions, increased (i.e., standard deviations decreased) with increasing oxidation state. These findings correlate with the calculated cage-correlation times which were largest for Cr^{3+}, shortest for Cr^0, and intermediate for Cr^{2+}. The results suggest an increasing tendency for the formation of more stable Cr-F associates with increasing oxidation state.

A significant finding in the present work is that the Cr solute atoms in the associate forming $2LiF-BeF_2$ and $2LiF-AlF_3$ systems solvate not only with dissociated F^- anions, but also with F^- that are part of the oligomer structures. In particular, we find that the Cr solutes tend to incorporate into these oligomer structures by joining (cross-linking) host oligomers, thereby increasing their average length. The results suggest that the common picture of solvation by dissociated F^- anions is oversimplified and the important role of the host oligomer structures must be considered. When the concentration of dsF is in equilibrium with unsaturated reservoirs of ucC and brF, the solute has acid-base buffering capacity that can produce dsF for the solvation of Cr solutes. Furthermore, Cr incorporation into an oligomer structure allows it to solvate without needing to consume dissociated F^- or take F^- from the existing oligomers. The results thus suggest a more complex picture of Cr solvation beyond the traditional picture that emphasizes the

correlation with fluroacidity as a measure of the dissociated fluoride concentration. This simple picture of Cr solvation is further challenged by the observation in the present simulations of highly stable Cr-Be and Cr-Al cation neighbors for the case of Cr^0 solutes that form without bridging F^- anions, and at bond lengths suggesting direct bonding. An additional factor that has not been considered in the present work is the role of Cr-Cr interactions. Recent work has shown that transition metal solutes can form dimers and trimers in molten fluorides [94], which suggests that our picture of Cr solvation may change when not in the dilute limit. A final factor that has not been considered in the present work is the evolution of Cr solvation structures with temperature. This effect is of particular importance to corrosion in molten salt systems where temperature gradients are the drivers for corrosion. Significant changes in solvation structure with temperature would lead to a higher rate of corrosion.

The present results provide important insights into the mechanisms that underlie molten-salt corrosion of metals. As the oligmer distribution of the salt must accommodate the Cr solute in order for dissolution to take place, changes in that distribution will impact both the kinetics of dissolution and the most stable Cr charge state. For example, the molten salt double layer (DL) may significantly affect these by drastically changing the local short- and medium-range order. If the DL leads to longer and more rigid oligomers, then Cr solutes will have to displace such an oligomer network in order to dissolve, potential leading to suppressed dissolution kinetics. Furthermore, the DL may lead to extremely complex transport phenomena, as Cr must hop between oligomeric environments, with or without its coordinating fluorides. Lastly, the possibility for Cr^0 to form direct bonds with ionized cations in the salt may provide a second mechanism for dissolution, whereby Cr^0 is pulled from the surface, with oxidation occurring after dissolution is complete.

6. Author contributions

NW, RS, and MA conceptualized the project. NW performed AIMD calculations with feedback from MA. NW analyzed the AIMD with feedback from both RS and MA. RS provided the chemical interpretation of the AIMD results. HW provided the literature background on fluoroacidity and chromium solvation. RS and HW developed the fluoroacidity discussion. All authors worked on the writing the manuscript together.

Declaration of Competing Interest

At the time at which the article is published, one of the authors of this manuscript has interests in or relationships with entities that are commercializing nuclear technology. The content of this manuscript or the direction of the research presented herein was not influenced by these entities, nor by the authors' relationships with these entities.

Acknowledgements

This research was supported as part of FUTURE (Fundamental Understanding of Transport Under Reactor Extremes), an Energy Frontier Research Center funded by the U.S. Department of Energy (DOE), Office of Science, Basic Energy Sciences (BES). The simulations made use of computing resources from the Extreme Science and Engineering Discovery Environment (XSEDE), which is supported by National Science Foundation Grant No. ACI-1548562. HW also acknowledges the support of the University of California, Berkeley, Chancellor's Fellowship.

Appendix A. Supplementary material

Supplementary data associated with this article can be found, in the online version, at https://doi.org/10.1016/j.molliq.2021.116351.

References

[1] James J. Laidler et al., Development of pyroprocessing technology, Progress in Nuclear Energy 31 (1–2) (1997) 131–140.
[2] Jerome Serp et al., The molten salt reactor (MSR) in generation IV: overview and perspectives, Progress in Nuclear Energy 77 (2014) 308–319.
[3] Charalampos Andreades et al., Design Summary of the Mark-I Pebble-Bed, Fluoride Salt-Cooled, High-Temperature Reactor Commercial Power Plant, Nuclear Technology 195 (2016) 223–238.
[4] Charles W. Forsberg, Per F. Peterson, Paul S. Pickard, Molten-salt-cooled advanced high-temperature reactor for production of hydrogen and electricity, Nuclear Technology 144 (3) (2003) 289–302.
[5] E.S. Bettis et al., The aircraft reactor experiment–operation, Nuclear Science and Engineering 2 (6) (1957) 841–853.
[6] Paul N Haubenreich and JR Engel. Experience with the molten-salt reactor experiment. In: Nuclear Applications and technology 8.2 (1970), pp. 118–136.
[7] Tim Abram, Sue Ion, Generation-IV nuclear power: A review of the state of the science, Energy Policy 36 (12) (2008) 4323–4330.
[8] C.F. Baes Jr., The chemistry and thermodynamics of molten salt reactor fuels, Journal of Nuclear Materials 51 (1) (1974) 149–162.
[9] K. Sridharan, T.R. Allen, Corrosion in molten salts, In: Molten salts chemistry. From lab to applications. (2013) 241–267.
[10] Luke C Olson et al., Materials corrosion in molten LiF-NaF-KF salt, Journal of Fluorine Chemistry 130 (1) (2009) 67–73.
[11] W. Zhou, Y. Yang, G. Zheng, et al., Proton irradiation-decelerated intergranular corrosion of Ni-Cr alloys in molten salt, Nature Communications 11 (2020) 3430.
[12] Luke Olson et al., Intergranular corrosion of high temperature alloys in molten fluoride salts, Materials at High Temperatures 27 (2) (2010) 145–149.
[13] C.T. Ewing, J.R. Spann, R.R. Miller, Radiant Transfer of Heat in Molten Inorganic Compounds at High Temperatures, Journal of Chemical Engineering Data 7 (2) (1962) 246–250.
[14] Ethan S. Chaleff et al., Ab-Initio Calculation of Spectral Absorption Coefficients in Molten Fluoride Salts with Metal Impurities, Nuclear Technology 204 (1) (2018) 59–65.
[15] CM Blood. Solubility and stability of structural metal difluorides in molten fluoride mixtures. Tech. rep. ORNL-TM-760. Oak Ridge National Lab. (ORNL), Oak Ridge, TN (United States), 1964.
[16] AW Savolainen. Aircraft Nuclear Propulsion Project Quarterly Progress Report for Period Ending June 10, 1955. Tech. rep. ORNL-1947. Oak Ridge National Lab. (ORNL), Oak Ridge, TN (United States), 1955.
[17] W.H. Jordan. Aircraft Nuclear Propulsion Project Quarterly Progress Report for Period Ending December 31, 1956 - ORNL-2221. Tech. rep. Oak Ridge National Lab. (ORNL), Oak Ridge, TN (United States), 1957.
[18] J. Redman. Aircraft Nuclear Propulsion Project Quarterly Progress Report ORNL-2157. Tech. rep. Oak Ridge National Lab. (ORNL), Oak Ridge, TN (United States).
[19] Aircraft Nuclear Propulsion Project. Tech. rep., ORNL-2106., Tech. Oak Ridge National Lab. (ORNL, Oak Ridge, TN (United States, 1967.
[20] JD Redman. Aircraft Nuclear Propulsion Project Quarterly Progress Report for Period Ending June 10, 1956. Tech. rep. ORNL-2106. Oak Ridge National Lab. (ORNL), Oak Ridge, TN (United States) 1956, pp. 96–103.
[21] Qiu Jie et al., Speciation study of chromium corrosion product in molten LiF-NaF-KF salt, Nuclear Science and Technology 26 (6) (2015), 60602–060602.
[22] F DavidWilliams, M LouisToth, T KevinClarno, et al., Assessment of Candidate Molten Salt Coolants for the Advanced High Temperature Reactor (AHTR), in: Tech. rep., ORNL/TM-2006/12., Oak Ridge National Lab. (ORNL, Oak Ridge, TN (United States, 2006.
[23] J. Redman. Molten-Salt, Reactor Program Quarterly Progress Report for Period Ending October 31, 1958, in: Tech. rep., ORNL-2626., Oak Ridge National Lab. (ORNL, Oak Ridge, TN (United States, 1959.
[24] Yiyang Liu et al., Corrosion of Cr in molten salts with different fluoroacidity in the presence of CrF3, Corrosion Science 169 (2020) 108636.
[25] A.D. Pelton et al., The modified quasichemical model I-Binary solutions, Metallurgical and Materials Transactions B 31 (4) (2000) 651–659.
[26] Pelton, D. Arthur, Chartrand. Patrice, The modified quasi-chemical model: Part II. Multicomponent solutions, Metallurgical and Materials Transactions A 32 (6) (2001) 1355–1360.APA.
[27] Patrice Chartrand, D. Pelton Arthur, The modified quasi-chemical model: Part III. Two sublattices, Metallurgical and Materials Transactions A 32 (6) (2001) 1397–1407.
[28] Pelton, D. Arthur, Patrice Chartrand, Eriksson. Gunnar, The modified quasi-chemical model: Part IV. Two-sublattice quadruplet approximation, Metallurgical and Materials Transactions A 32 (6) (2001) 1409–1416.APA.
[29] O. Benes, R.J.M. Konings, Thermodynamic evaluation of the (LiF+ NaF+ BeF2+ PuF3) system: An actinide burner fuel, Journal of Chemical Thermodynamics 41 (10) (2009) 1086–1095.

[30] SalanneMathieu et al., A first-principles description of liquid BeF2 and its mixtures with LiF: 2. Network formation in LiF– BeF2, The Journal of Physical Chemistry B 110 (23) (2006) 11461–11467.
[31] L.M. Toth, J.B. Bates, G.E. Boyd, Raman spectra of Be2F73-and higher polymers of beryllium fluorides in the crystalline and molten state, The Journal of Physical Chemistry 77 (2) (1973) 216–221.
[32] Olivier Pauvert et al., In situ experimental evidence for a nonmonotonous structural evolution with composition in the molten LiF- ZrF4 system, Journal of Physical Chemistry B 114 (19) (2010) 6472–6479.
[33] M.C. Abramo et al., Ionic radii and diffraction patterns of molten alkali halides, Journal of Chemical Physics 68 (6) (1978) 2889–2895.
[34] S. Biggin, J.E. Enderby, Comments on the structure of molten salts, Journal of Physics C: Solid State Physics 15 (11) (1982) L305.
[35] RL McGreevy and L Pusztai. The structure of molten salts. In: Proceedings of the Royal Society of London. Series A: Mathematical and Physical Sciences 430.1878 (1990), pp. 241–261.
[36] Mathieu Salanne et al., Heat-transport properties of molten fluorides: Determination from first-principles, Journal of Fluorine Chemistry 130 (1) (2009) 38–44.
[37] Mathieu Salanne et al., Calculation of activities of ions in molten salts with potential application to the pyroprocessing of nuclear waste, Journal of Physical Chemistry B 112 (4) (2008) 1177–1183.
[38] A.E. Gheribi et al., Prediction of the thermophysical properties of molten salt fast reactor fuel from first-principles, Molecular Physics 112 (9–10) (2014) 1305–1312.
[39] Capelli, E., O. Beneš, and R. J. M. Konings. "Thermodynamic assessment of the LiF–NaF–BeF2–ThF4–UF4 system." *Journal of Nuclear Materials* 449.1-3 (2014): 111-121.
[40] Mathieu Salanne, Polarization effects in ionic solids and melts, Molecular Physics 109 (19) (2011) 2299–2315.
[41] Eveline M Adams, IR McDonald, and K Singer. Collective dynamical properties of molten salts: molecular dynamics calculations on sodium chloride. In: Proceedings of the Royal Society of London. A. Mathematical and Physical Sciences 357.1688 (1977), pp. 37–57.
[42] Marie-Louise Saboungi et al., Molecular dynamics studies of complexing in binary molten salts with polarizable anions: MAX4, The Journal of chemical physics 88 (9) (1988) 5818–5823.
[43] Marie-Louise Saboungi, ANEESUR Rahman, and Milton Blander. Molecular dynamics studies of complexing in binary molten salts. I. Molten MAX4. In: The Journal of chemical physics 80.5 (1984), pp. 2141-2150.
[44] Milton Blander, Marie-Louise Saboungi, Aneesur Rahman, Molecular dynamics studies of complexing in binary molten salts. II. Molten M3AX6 and MA3X10, The Journal of chemical physics 85 (7) (1986) 3995–4004.
[45] Vincent Sarou-Kanian et al., Diffusion coefficients and local structure in basic molten fluorides: in situ NMR measurements and molecular dynamics simulations, Physical Chemistry Chemical Physics 11 (48) (2009) 11501–11506.
[46] Leslie C Dewan et al., Molecular dynamics simulation of the thermodynamic and transport properties of the molten salt fast reactor fuel LiF-ThF4, Journal of nuclear materials 434 (1-3) (2013) 322–327.
[47] Francis Hutchinson, Mark Wilson, Paul A Madden, A unified description of MCl3 systems with a polarizable ion simulation model, Molecular Physics 99 (10) (2001) 811–824.
[48] William J Glover, Paul A Madden, Raman spectra of ionic liquids: a simulation study of LaC13 and its mixtures with alkali chlorides, The Journal of chemical physics 121 (15) (2004) 7293–7303.
[49] Y. Okamoto, P.A. Madden, K. Minato, X-ray diffraction and molecular dynamics simulation studies of molten uranium chloride, Journal of nuclear materials 344 (1-3) (2005) 109–114.
[50] M. Salanne et al., Modeling of Molten Salts, in: Frederic Lantelme, Henri Groult (Eds.), Molten Salts Chemistry, Elsevier, Oxford, 2013, pp. 1–16.
[51] Amelia Bengtson et al., First-principles molecular dynamics modeling of the LiCl-KCl molten salt system, Computational materials science 83 (2014) 362–370.
[52] A. Klix, A. Suzuki, T. Terai, Study of tritium migration in liquid Li2BeF4 with ab initio molecular dynamics, Fusion engineering and design 81 (1-7) (2006) 713–717.
[53] Nam, Hyo On, Morgan. Dane, Redox condition in molten salts and solute behavior: A first-principles molecular dynamics study, Journal of Nuclear Materials 465 (2015) 224–235.
[54] Jianqi Xi et al., Corrosion of Si, C, and SiC in molten salt, Corrosion Science 146 (June 2019) (2018) 1–9.
[55] H.O. Nam et al., First-principles molecular dynamics modeling of the molten fluoride salt with Cr solute, Journal of Nuclear Materials 449 (1–3) (2014) 148–157.
[56] L. Martinez et al., Packmol: A Package for Building Initial Configurations for Molecular Dynamics Simulations, Journal of computational chemistry 30 (13) (2009) 2157–2164.
[57] Steve Plimpton, Fast Parallel Algorithms for Short-Range Molecular Dynamics, Journal of Computational Physics 117 (6) (1997) 1–42.
[58] Shuichi Nose, A unified formulation of the constant temperature molecular dynamics methods, The Journal of chemical physics 81 (1) (1984) 511–519.
[59] William G Hoover, Canonical dynamics: Equilibrium phase-space distributions, Physical review A 31 (3) (1985) 1695.
[60] G. Kresse, D. Joubert, From ultrasoft pseudopotentials to the projector augmented-wave method, Physical Review B 59 (3) (Jan. 1999) 1758–1775.
[61] G. Kresse, J. Furthmuller, Efficient iterative schemes for ab initio total-energy calculations using a plane-wave basis set, Physical Review B - Condensed Matter and Materials Physics 54 (16) (1996) 11169–11186.
[62] John P. Perdew, Kieron Burke, Matthias Ernzerhof, Generalized gradient approximation made simple, Physical Review Letters 77 (18) (1996) 3865–3868.
[63] Stefan Grimme, Semiempirical GGA-type density functional constructed with a long-range dispersion correction, Journal of computational chemistry 27 (15) (2006) 1787–1799.
[64] Jun Ding et al., Second-nearest-neighbor correlations from connection of atomic packing motifs in metallic glasses and liquids, Scientific reports 5 (1) (2015) 1–9.APA.
[65] J. Eran Rabani, Daniel Gezelter, B.J. Berne, On the Temperature Dependence of Cooperative Relaxation Properties in Glass-Forming Liquids, Journal of Chemical Physics 107 (1997) 139.
[66] M. O'Keeffe, A proposed rigorous definition of coordination number, Ada Crystallo-graphica Section A: Crystal Physics, Diffraction, Theoretical and General Crystallography 35 (5) (1979) 772–775.
[67] S. Cantor et al., Reactor Chemistry Devision, Oak Ridge National Lab, ORNL-TM-2316., ORNL, Oak Ridge, TN (United States, 1968, p. 55.
[68] B.C. Blanke et al., *Density and Viscosity of Fused Mixtures of Lithium, Beryllium, and Uranium Fluorides*. No, Mound Lab, Miamisburg, Ohio, 1956.
[69] B J Sturm, Reactor Chemistry Division Annual Progress Report. Tech. rep. ORNL-3789. Oak Ridge National Lab (ORNL). (1965) 83.
[70] Robert J Heaton et al., A first-principles description of liquid BeF2 and its mixtures with LiF: 1. Potential development and pure BeF2, Journal of Physical Chemistry B 110 (23) (2006) 11454–11460.
[71] F. Vaslow, A.H. Narten, Diffraction pattern and structure of molten BeF2-LiF solutions, Journal of Chemical Physics 59 (9) (1973) 4949–4954.
[72] Jianxing Dai et al., Molecular dynamics studies of the structure of pure molten ThF4 and ThF4-LiF-BeF2 melts, Journal of Molecular Liquids 211 (2015) 747–753.
[73] B. Shadrack Jabes, Manish Agarwal, Charusita Chakravarty, Structure and transport properties of LiF-BeF 2 mixtures: Comparison of rigid and polarizable ion potentials, Journal of Chemical Science 124 (1) (2012) 261–269.
[74] George J. Janz, Thermodynamic and transport properties for molten salts: correlation equations for critically evaluated density, surface tension, electrical conductance, and viscosity data, Journal of Physical and Chemical Reference Data 17 (1988).
[75] W.R. Grimes et al., Reactor Chemistry Division Annual Progress Report for Period Ending December 31, 1965, in: Tech. rep., ORNL-3913., Oak Ridge National Lab. (ORNL), Oak Ridge, TN (United States), 1965, p. 29.
[76] V. Dracopoulos, G.N. Papatheodorou, Isotropic and anisotropic Raman scattering from molten alkali-metal fluorides, Physical Chemistry Chemical Physics 2 (9) (2000) 2021–2025.
[77] Vincent Lacassagne et al., Structure of high-temperature NaF- A1F3- A12O3 melts: a mult-inuclear NMR study, Journal of Physical Chemistry B 106 (8) (2002) 1862–1868.
[78] Brooker, H. Murray, et al., Raman Study of the hexafluoroaluminate ion in solid and molten FLINAK, Inorganic chemistry 39 (16) (2000) 3682–3689.
[79] B. Gilbert, T. Materne, Reinvestigation of Molten Fluoroaluminate Raman Spectra: The Question of the Existence of A1F52-Ions, Applied Spectroscopy 44 (2) (1990) 299–305.
[80] Min Tan et al., Thermodynamic Investigation on Ionic Structure and Electrical Conductivity of Molten NaF-AlF3 Salts, Journal of The Electrochemical Society 167 (2) (2020) 023503.
[81] Hu. Xian-wei et al., Raman spectra of ionic structure for acidic NaF-AlF3 melts, The Chinese Journal of Nonferrous Metals 18 (10) (2008) 1914–1919.
[82] Ernest W Dewing. Models of Halo-Aluminate Melts. In: Proceedings - The Electrochemical Society. Vol. 1986. 1986, p. 261.
[83] MachadoKelly et al., Study of NaF–AlF3 Melts by Coupling Molecular Dynamics, Density Functional Theory, and NMR Measurements, The Journal of Physical Chemistry C 121 (19) (2017) 10289–10297.
[84] Kelly Machado et al., Structural, Dynamic, and Thermodynamic Study of KF-A1F3 Melts by Combining High-Temperature NMR and Molecular Dynamics Simulations, The Journal of Physical Chemistry C 123 (4) (2019) 2147–2156.
[85] C.F. Baes Jr., A polymer model for BeF2 and SiO2 melts, Journal of Solid State Chemistry 1 (2) (1970) 159–169.
[86] Sergey V Sukhomlinov, Martin H Muser, Determination of accurate, mean bond lengths from radial distribution functions, The Journal of chemical physics 146 (2) (2017) 024506.
[87] Kristin Persson. Materials Data on AlSCr (SG:139) by Materials Project. An optional note. Feb. 2016.
[88] Kristin Persson. Materials Data on Be2Cr (SG:194) by Materials Project. An optional note. Feb. 2016.
[89] M. Kergoat et al., Investigation on fluoroacidity of molten fluorides solutions in relation with mass transport, Electrochimica Acta 120 (2014) 258–263.
[90] Ernest W. Dewing, The Effect of Additives on Activities in Cryolite Melts, Metallurgical Transactions B 20B (October) (1989) 675–677.
[91] Bernard Piriou, J.J. Videau, J. Portier, Raman spectroscopic studies of aluminium flu-oroberyllate glasses, Journal of Non-Crystalline Solids 46 (1) (1981) 105–110.
[92] J.A. Duffy, Optical basicity: A practical acid-base theory for oxides and oxyanions, Journal of chemical education 73 (12) (1996) 1138.

[93] S.J. Cromer. Aircraft Nuclear Propulsion Project Quarterly Progress Report for Period Ending June 10, 1956. Tech. rep. ORNL-2106. Oak Ridge National Lab. (ORNL), Oak Ridge, TN (United States), 1956.
[94] Austin David Clark et al., Complexation of Mo in FLiNaK Molten Salt: Insight from Ab Initio Molecular Dynamics, The Journal of Physical Chemistry B (2020).
[95] Dario Corradini, Paul A Madden, Mathieu Salanne, Coordination numbers and physical properties in molten salts and their mixtures, Faraday discussions 190 (2016) 471–486.
[96] Catherine Bessada et al., In situ NMR approach of the local structure of molten materials at high temperature, Comptes Rendus Chimie 9 (3–4) (2006) 374–380.
[97] Catherine Bessada et al., High temperature NMR approach of mixtures of rare earth and alkali fluorides: An insight into the local structure, Journal of Fluorine Chemistry 130 (1) (2009) 45–52.
[98] Anne BieberLaure et al., Fluoroacidity evaluation in molten salts, Electrochimica acta 56 (14) (2011) 5022–5027.
[99] S Jaskierowicz et al. Attempt to classify various molten fluoride mixtures according to their solvation powers regarding metal fluorides. In: Proceedings of the First ACSEPT International Workshop Lisbon, Portugal, 31 March - 2 April 2010 (2010).
[100] Mickael Kergoat. Evaluation de la fiuoroacidite en milieux de sels fondus. PhD thesis. Universite de Toulouse, Universite Toulouse Ill-Paul Sabatier, 2014.